Politecnico di Torino

M.Sc in Aerospace Engineering

Modeling, Dynamics and Control of Planetary Smart Boomerangs

Jet Propulsion Laboratory
California Institute of Technology

Mentors:
Dr. Marco B. Quadrelli
Dr. Adrian Stoica
Jet Propulsion Laboratory
Co-Mentor:
Dr. Federico Rossi
Jet Propulsion Laboratory

Supervisor:
Prof. Eugenio Brusa

Candidate:
Davide Di Santis

JPL Visiting Student Research Program

Academic Year 2023-2024

This research was carried out at the Jet Propulsion Laboratory, California Institute of Technology, and was sponsored by JVSRP (JPL Visiting Student Research Program) and the National Aeronautics and Space Administration (80NM0018D0004).

Sommario

In un tentativo di ampliare le capacità dei boomerang classici, Adrian Stoica ha introdotto il concetto di "Smart Boomerang". Questo boomerang regola le sue superfici di controllo del volo o altre caratteristiche interne per ottenere traiettorie molto più complesse di quelle realizzabili con i boomerang standard. Esso potrebbe persino terminare il suo volo in un punto diverso da quello in cui è stato lanciato, il che è utile se deve essere recuperato da un veicolo in movimento. Sui pianeti con atmosfera, uno Smart Boomerang potrebbe essere lanciato automaticamente da una piattaforma atmosferica, come un pallone aerostatico su Venere o Titano, o da una piattaforma terrestre, ritornando al lanciatore nella sua nuova posizione. In questo modo, può eseguire osservazioni o campionamenti. Questo comporta alcuni vantaggi e svantaggi rispetto a un drone, come ad esempio un elicottero. Questo lavoro descriverà uno strumento di simulazione sviluppato per prevedere la traiettoria di un boomerang, dati i suoi parametri di progettazione e le condizioni di lancio. Sono state derivate e testate in simulazione le equazioni non lineari del moto per la dinamica di volo del boomerang. I risultati sono stati convalidati dal confronto con traiettorie misurate in test sperimentali. Il tool sviluppato consente inoltre di analizzare gli effetti del vento.
Viene quindi implementato un controllore PID per consentire l'inseguimento di traiettorie desiderate predeterminate e vengono confrontati diversi meccanismi per ottenere artificialmente un cambio di traiettoria a mezz'aria. Questo lavoro è stato svolto a seguito di alcuni test sperimentali, dove si è utilizzato un prototipo di Smart Boomerang, il cui design verrà delineato. Infine, verranno presentate considerazioni sul problema della State Estimation. In sintesi, questo lavoro amplia il concetto di Smart Boomerang analizzando la sua dinamica e la possibilità di controllo della traiettoria. Il modello sviluppato funziona come strumento alternativo e complementare ai test sperimentali. Esso permette di raccogliere dati essenziali sulla fattibilità delle missioni con Smart Boomerang in modo efficace dal punto di vista dei tempi e dei costi.

Abstract

In an attempt to expand the capabilities of classic boomerangs, Adrian Stoica introduced the concept of a "Smart Boomerang". This boomerang adjusts its flight control surfaces or other internal characteristics to achieve much more complex trajectories than those feasible with standard boomerangs. It could even end its flight at a different location from where it was launched, which is useful if it is to be retrieved by a vehicle in motion. On planets with atmospheres, such a Smart Boomerang could be launched automatically from an atmospheric platform, such as a balloon on Venus or Titan, or from a ground platform, returning to the launcher at its new location. Thus, it can perform observations or even sampling. This has some advantages and disadvantages compared to a drone, such as a helicopter.

This work will describe a simulation tool developed to predict a boomerang's trajectory, given its design parameters and launch conditions. To further analyze the capabilities of this system, non-linear equations of motion for boomerang flight dynamics have been developed and tested in simulation. The results were validated by comparison with trajectories measured in experimental tests. The models further allow to analyze wind effects.

A PID controller is then implemented to enable the tracking of pre-determined desired trajectories, and different mechanisms to artificially achieve a mid-air trajectory change are compared. This work was carried out as a consequence of experimental tests that were run throwing a Smart Boomerang prototype, the design of which will be presented.

Finally, considerations about the state estimation problem are presented.

In summary, this work expands the concept of Smart Boomerangs by exploring their dynamics and the possibility of controlling their trajectories. The developed model works as an alternative yet complementary tool to experimental tests. It enables gathering essential data about the feasibility of Smart Boomerang Missions in time- and cost-effective manners.

Ringraziamenti

Ringrazio il Professor Eugenio Brusa, che mi ha permesso di svolgere questa tesi nel contesto di un'avventura fantastica caratterizzata da un motto: *Dare Mighty Things*. Grazie ai miei mentori: Dr. Adrian Stoica e Dr. Marco B. Quadrelli, che mi hanno fatto capire cosa questo motto significasse, assieme a tanti altri ingegneri del JPL con cui ho avuto modo di prendere un caffé o pranzare: Federico Rossi, Stefano Campagnola, Kalind Carpenter, Marco Dolci, e molti altri.
Mi ritengo abbastanza fortunato da avere diversi gruppi di persone da ringraziare, e lo farò elencando i gruppi e le persone senza seguire alcun ordine particolare.
Grazie alla mia famiglia: a mio padre, che mi ha trasmesso perseveranza e instancabilità nel lavoro; a mia madre, per avermi trasmesso una sensibilità che spesso nascondo, e aver piantato in me questa passione per lo spazio e l'ignoto che mi ha portato a vivere le avventure più belle della mia vita; a Cosimo e Clelia, per il loro amore e supporto; e a Serena, per essermi sempre stata vicino, essendo quasi una seconda mamma, e per tutte le uscite tra Milano e Torino.
Grazie ai miei amici di Taranto: Francesco, Mario, Federico, Fra, Stefano, Alessio, Gabriele e Leandro. Non sapete quanto è stato importante distrarmi con voi dall'università, compiendo imprese virtuali epiche in una Los Angeles miniaturizzata o alla guida di automobili in un campo da calcio o alla caccia di fantasmi, guardando anime e andando a spasso per la nostra amata Taranto.
Grazie ai miei amici "torinesi": Maradon, coinquilino storico e grande cuoco; Anthony, per avermi permesso di insegnarti così tanto; Amadeo, e tutto il supporto che fornisci alla minima richiesta; Francesco P., con tutti i nostri pranzi in mensa e avventure in DRAFT; Katia, per i frozen yogurt all'Intelligenza Artificiale; Riccardo, Tony, Valentina, Viviana, per la preziosa amiciza. E grazie al team DRAFT e ai suoi fondatori Dario, Francesco, Luigi, per il supporto e la guida negli anni. Siete un'ispirazione per la mia carriera, e grazie a questo team e a tutte le persone che lo compongono ho sbloccato tante abilità ingegneristiche e interpersonali, oltre che trovato amicizie di valore. Grazie al club Toastmasters

per la piacevole alternativa alla mia costante (e comunque piacevolissima) immersione in argomenti tecnici. A Grazia. E a Massimo. Avrei voluto raccontarti le mie avventure americane più assurde. Spero tu le abbia viste, ovunque tu sia.
Grazie a Cri e Matt, per le lunghe chiacchierate a distanza e per i bellissimi e troppo sporadici incontri di persona.
Grazie ai miei amici "americani": Pierluigi, con cui sono andato a bussare alla porta dei più importanti ingegneri di JPL chiedendo una chiacchierata; Camilla, Marzo e Matteo, per tutte le risate e avventure che abbiamo condiviso tra meme, California e Nevada (Pahrump nel cuore); Letizia, per quanto abbiamo preso in giro Elior, e per tutti gli scherzi, battute e amichevoli insulti "cafoni" che hai subito e (malamente) incassato (quantità e cafonaggine dei quali sono direttamente proporzionali al mio affetto); Elior, compagno di banco, black humor e vittima di fantasiosi e amichevoli ma incondivisibili insulti (sempre direttamente proporzionali al mio affetto); Allie, powerbank per le mie batterie sociali; gli amici "hawaiiani" Carmine, Dario, Emma, Fredrik, Fernando e Tom (Caronte accompagnatore di anime perdute verso l'inferno di LAX), per la vacanza più bella della mia vita. E Simone e Mario, per la vostra preziosa amicizia, per le avventure in metro e al JPL e in tre o forse quattro stati degli US. Non immaginate quanto conoscervi e avervi come amici mi abbia insegnato. Ci sono tante altre persone con cui ho condiviso cene, hamburger per cui sono stato grato di avere un'assicurazione sanitaria, tramonti, scene mozzafiato, pranzi sotto il sole cocente del mall del JPL: grazie Hope, Anoushka, Gregory, Manthan, Aurelio, Ioan, Grzegorz, Juan, Davide 2 e 3, la crew francese e...
tante, tante altre persone incredibili - mi spiace se il vostro nome non è qui, ma avete certamente un posto nel mio cuore.

Acknowledgements

Many thanks to Professor Eugenio Brusa, who enabled me to carry out this thesis work in the setting of a fantastic adventure characterized by a motto: *Dare Mighty Things*. Thanks to my mentors Dr. Adrian Stoica and Dr. Marco B. Quadrelli, who taught me what this motto meant, along with so many other JPL engineers with whom I had the opportunity to have coffee or lunch: Federico Rossi, Stefano Campagnola, Kalind Carpenter, Marco Dolci, and many others.
I consider myself lucky enough to have several groups of people to thank, and I will do so by listing the groups and people in no particular order.
Thanks to my family: to my father, who has passed on to me perseverance and tirelessness in my work; to my mother, for passing on to me a sensitivity that I often hide, and planting in me this passion for space and the unknown that has led me to the most beautiful adventures of my life; to Cosimo and Clelia, for their love and support; and to Serena, for always being by side, being almost a second mom, and for all the outings between Milan and Turin.
Thanks to my friends from Taranto: Francesco, Mario, Federico, Fra, Stefano, Alessio, Gabriele and Leandro. You were a very much-needed distraction from university, and words cannot describe how much fun I had performing epic virtual feats in a miniaturized Los Angeles, driving cars in a soccer field, or hunting ghosts, watching anime, and walking around our beloved Taranto.
Thank you to my Turin friends: Maradon, historical roommate and great cook; Anthony, for allowing me to teach you so much; Amadeo, and all the support you provide at the slightest request; Francesco P., with all our lunches in the cafeteria and adventures in DRAFT; Katia, for the AI-powered frozen yogurts; Riccardo, Tony, Valentina, Viviana, for the precious friendships. And thanks to the DRAFT team and its founders Dario, Francesco, and Luigi, for the support and guidance over the years. You are an inspiration for my career: DRAFT and all its members helped me unlock so many engineering and interpersonal skills, as well as find valuable friendships. Thanks to the Toastmasters club for the pleas-

ant alternative to my constant (and still very enjoyable) immersion in technical topics. To Grazia. And to Massimo. I wish I could have told you my wildest American adventures. I hope you have seen them, wherever you are.
Thanks to my "American" friends: Pierluigi, with whom I went knocking on the door of JPL's most important engineers asking for a chat; Camilla, Marzo and Matteo, for all the laughs and adventures we shared among memes, California, and Nevada (Pahrump forever); Letizia, for teaming up in making fun of Elior, and for all the jokes and (friendly) insults you (badly) endured (quantity and boorishness of which are directly proportional to my affection); Elior, fellow desk-mate, black humor-mate and victim of creative and not-shareable friendly insults (again, directly proportional to my affection); Allie, fellow introvert and battery pack for my social batteries; "Hawaiian" friends Carmine, Dario, Emma, Fredrik, Fernando and Tom (Charon escort of lost souls to the hell of LAX), mahalo for the best vacation of my life. And Simone and Mario, for your precious friendship, for the adventures in the metro and at JPL and in three or maybe four states in the US. You cannot imagine how much getting to know you and having you as friends has taught me. There are so many other people with whom I shared dinners, hamburgers for which I was grateful to have health insurance, sunsets, breathtaking views, and lunches under the blazing sun at the JPL mall: thank you Hope, Anoushka, Gregory, Manthan, Aurelio, Ioan, Grzegorz, Juan, David 2 and 3, the French crew, and...
many, many other incredible people - sorry if your name is not here, but you certainly have a place in my heart.

Disclaimer

Reference herein to any specific commercial product, process, or service by trade name, trademark, manufacturer, or otherwise, does not constitute or imply its endorsement by the United States Government or the Jet Propulsion Laboratory, California Institute of Technology.

Contents

List of Figures

List of Tables

Chapter 1

Introduction

This work is inserted in the framework of developing a new technology concept carried on at the Jet Propulsion Laboratory in California as an affiliate of the Robotics Modeling and Simulation section. Figure 1.1 shows a synthetic system-level scheme of a Smart Boomerang Platform

The idea is to develop boomerangs capable of changing their trajectory in flight. An example of a Smart Boomerang trajectory is represented in figure 1.2. Such flying vehicles could be used as probes for atmospheric sampling on celestial bodies with dense atmospheres such as Venus or Titan. A launch-and-capture platform would be able to operate the boomerang probes, which in turn would be powered only by the energy imparted at launch.

The unique characteristic of a boomerang is that, after launch, it tends to naturally return to the initial launch position: this is an advantage when compared to other flying probes like helicopter drones, which present a large battery, require high-performance motors, and equip a complex electronic architecture.

A boomerang could be enhanced by simple electronic equipment, essential for trajectory control. The "Smart Boomerang" enhancement is crucial to ensure that the aircraft returns to its launch platform even if disturbed by environmental perturbations like winds. Moreover, if the Smart Boomerang were to be thrown from a moving platform like an atmospheric balloon, it could be able to track it and precisely return to it. This would be particularly useful for sampling the atmosphere at different heights, whereas a balloon might present limited vertical mobility.

The thesis work leverages experimental tests and virtual simulations to define the high-level requirements for a Smart Boomerang Mission and provides tools to comprehend their strengths and limits. Before proceeding with the description

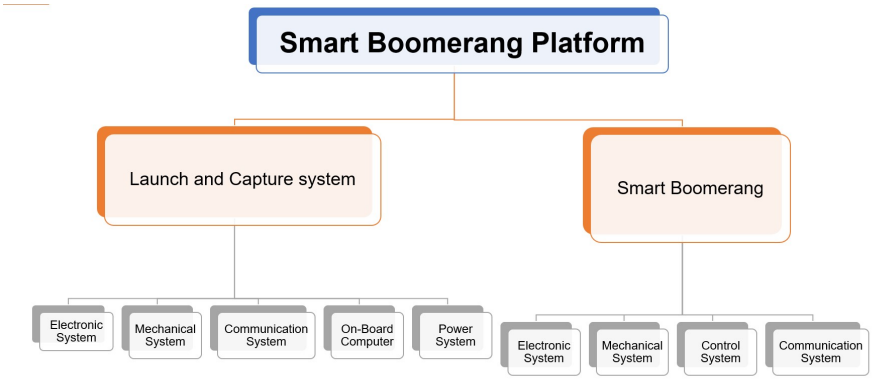

Figure 1.1: System-Level Scheme of a Smart Boomerang Platform

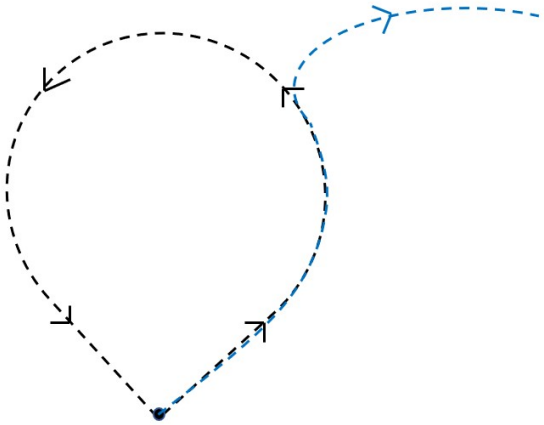

Figure 1.2: In black, the top-view of a returning trajectory of a standard boomerang. In blue, is an example of a trajectory achievable only by a Smart Boomerang

of the work done during the internship at NASA JPL, it is vital to provide an overview of standard boomerangs and their properties, as well as provide more details about Smart Boomerangs and their state-of-the-art.

Figure 1.3: Different boomerang configurations

1.1 Standard Boomerangs

Boomerangs are devices commonly associated with Australian Aborigines and are known for their capability to surprisingly return to their thrower after taking flight in the air. Historically, boomerang devices were also used by ancient Egyptians, natives of South India, and the Hopi Indians of Arizona [10].
It must be noted that the wooden curved boomerang that the Aborigines used for hunting was generally not of the returning type: it was a weapon used for its capability to fly in a straight line and strike a target with remarkable accuracy.
Boomerangs of the returning type correspond to only a small fraction of all the boomerangs that the Australians used. They are mainly used for recreational purposes but seldom find their use as decoys for hunting birds. Nowadays, returning boomerangs come in many shapes, presenting different numbers of wings and configurations that can resemble shapes like a V, a T, a Y, or a cross [10]. The model developed in this thesis allows us to study boomerangs with n-wings and different geometrical configurations. Figure 1.3 shows an example of different boomerang configurations.
Studies of the dynamical equations of the returning boomerang have been carried out in the past, with the main contributions given by Felix Hess [6] and Azuma et al [3]. The model developed in the thesis work is based on Azuma's publication and is further expanded introducing the effects of wind and the possibility of trajectory control.

1.2 Smart boomerangs

The idea behind the so-called smart boomerangs originated from Adrian Stoica, Ph.D, with the goal of enhancing the capabilities of standard boomerangs, allow-

ing them to achieve more complex trajectories. Many different methods can be thought to achieve trajectory control. Hereby, three are listed:

- **Controlling the wing pitch angle**: like an all-movable aircraft tail or the blades of a helicopter, the wings of the boomerang could be rotated (fig. 1.4) to change the aerodynamic forces acting on it. A collective pitch change would allow control of the magnitude of the lift and drag components, while cyclic pitch changes would allow to perform attitude adjustments. The latter capability would require motors capable of rotating the wing with a much higher frequency than the one of rotation for the boomerang; moreover, independent control of each wing would be required.
  A design solution for this type of boomerang will be presented: however, only collective pitch control will be achievable.

- **Controlling the wing dihedral angle:** By variating this angle (fig. 1.5), the angle of attack on the blades could be changed, thus modifying the aerodynamic forces' magnitude and direction. Moreover, the variation of the dihedral angle from 0 to $\Delta\beta$ results in a reduction of the radius of the boomerang flight disk. This design could be achieved by using servomotors that rotate the wings similarly to how the wing pitch rotation is achieved; however, its practical implementation might be a bit more difficult as each wing would require a dedicated servomotor.

- **Controlling the blade length:** varying the length of the blades (1.6) implies a change of the total wet surface, thus changing the total lift produced. However, this will also result in an inversely proportional variation of angular speed, as a consequence of the conservation of angular momentum, therefore the effects on trajectory might not be intuitive. A design was proposed during the Summer Internships carried out at NASA JPL in 2023, and will be briefly introduced in the following section.

Each of these control methods is modeled in the developed simulator, and considerations about the performance of each will be presented in chapter 5.

1.2.1 Previous work

The Smart Boomerang project started in during the Summer Internships 2023 hosted by NASA Jet Propulsion Laboratory. The interns Kimya R. Vakilian,

Figure 1.4: Variation of the wings' pitch angle

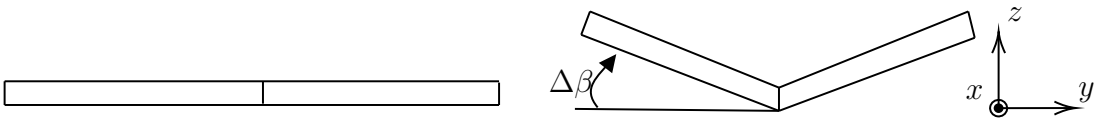

Figure 1.5: Variation of the wings' dihedral angle

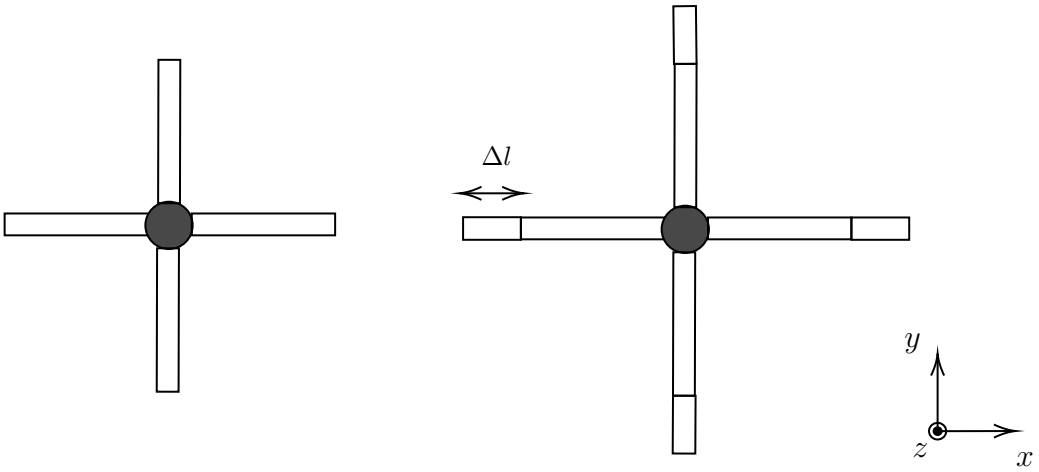

Figure 1.6: Variation of the wings' length

Nicholas M. Hennigan, Luke A. Cortez worked under the supervision of Dr. Adrian Stoica. Their main contributions were:

1. Analysis of boomerang flight equations to propose Smart Boomerang designs
2. Design and development of a Boomerang Launcher
3. Execution of experimental tests to gather data on the flight of Standard Boomerangs

Analysis of boomerang flight equations

A model developed by Vassberg [12] includes a formula to estimate a boomerang's flight path radius R_P:

$$R_P = \frac{6Isin\Phi_0}{\rho S C_{L0}}$$

where I is the mass moment of inertia, Φ_0 is the roll angle of the boomerang at launch, ρ is the air density, S the total wing surface of the boomerang, and C_{L0} the aerodynamic coefficient at zero angle of attack. Vassberg derived this formula for level circular flight at small angles of attack; throughout this work, these assumptions will not be considered, as a flying boomerang undergoes a large variation of altitude during flight, its trajectory is not a perfect circle, and flight happens at large angles of attack. However, the formula is useful to determine what design parameters influence the flight trajectory of the boomerang. Therefore, two Smart Boomerang configurations are proposed.
In the first case, by controlling the wing pitch angle of each wing (fig. 1.7), it is possible to act on the C_{L0} coefficient. The pitch variation is possible thanks to a servomotor which is connected to a main gear. In turn, the main gear is coupled with other beveled gears connected to each wing, so that when the servomotor spins each wing also rotates with it.
A second design was proposed (fig. 1.8), where the trajectory control is performed through changes in the blade length, and thus in the mass moment of inertia and total wing surface. In this case, a servomotor spins a disk, pierced with guides that push on spheres as the disk rotates. The spheres are connected to wing extensions, thus extending the total wing surface once the servomotor spins in a direction, and retracting them when spinning in reverse.
Another consideration was withdrawn about the design of boomerangs: considering that, for a rotating object, the rotational speed grows linearly with the

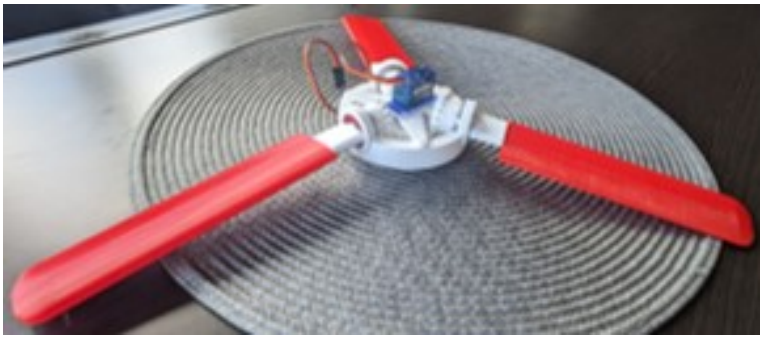

Figure 1.7: Proposed design of a controllable pitch Smart Boomerang

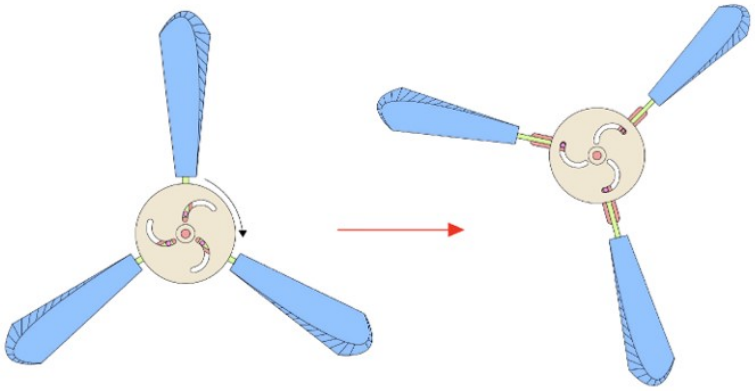

Figure 1.8: Proposed design of a controllable wing-length Smart Boomerang

distance from its center of rotation, and that the lift produced is directly proportional to the square of the flight velocity, it is possible to optimize wing design by designing wings that are narrow at the root and wider at the tip. This design is common in commercially available boomerangs (fig. 1.9).

Figure 1.9: Standard Boomerang with a narrower section at the root and a wider one at the tip

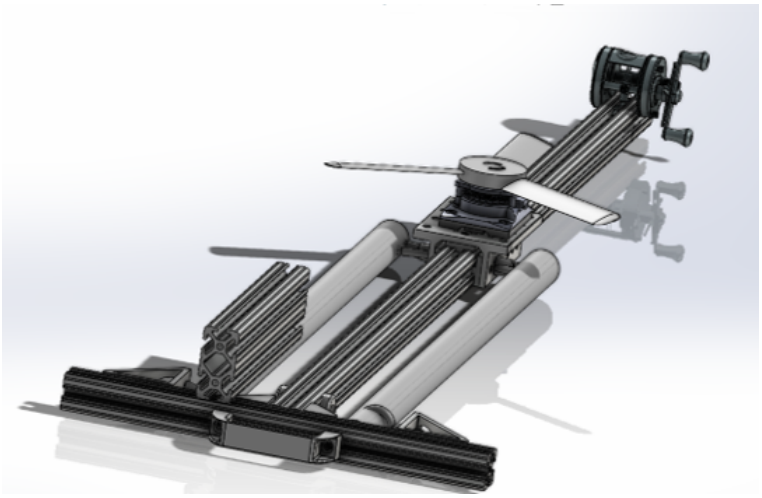

Figure 1.10: Launcher developed by the Summer Interns

Figure 1.11: Experimental launcher developed by Kimya Vakilian, Luke Cortez, Nick Hennigan

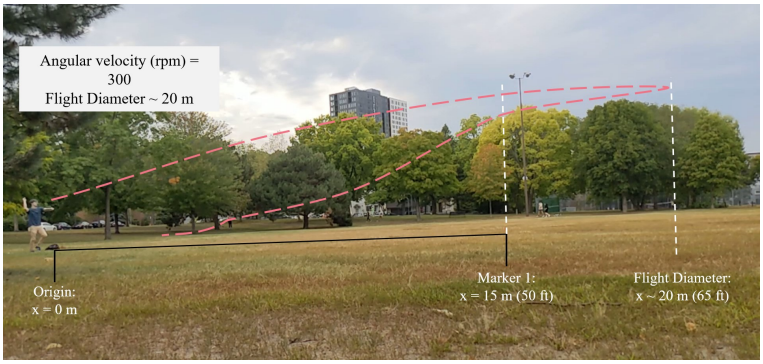

Figure 1.12: Example of experimental test

Design and development of a Boomerang Launcher

As shown in the scheme in figure 1.1, a Launch and Capture system is one of the subsystems needed for a Smart Boomerang Mission. The Summer Interns worked on developing a Launcher capable of throwing the boomerang with a mechanism similar to the one of a crossbow (fig. 1.10): a fishing line is used to load a spring which, when released, drags the slot on which the Boomerang is mounted. As the slot translates, gears make the boomerang spin at the same time.
An actual Launcher was built with Commercial Off-the-shelf components (fig. 1.11). However, it was hard to release the boomerang at the correct time, resulting in faulty launches. Moreover, there is no electronic control, making it hard to set a translational and rotational launch speed.

Experimental tests

Many experimental tests were run to compare the performance of different boomerang designs (fig. 1.12). The experimental setup included measuring the translational and rotational speed at launch using camera footage and exploiting environmental features for measuring the distance traveled. One of the experimental tests will be leveraged in the following chapters for the validation of the developed simulation tool. Regarding the experiments, the main conclusions drawn were:

- A boomerang with a cropped wing at the root is more easily thrown at higher RPMs due to the reduced mass and ends up flight with a smaller flight radius
- A boomerang with the same geometrical conditions but for a different wing

pitch angle will complete a returning trajectory with a smaller flight radius, proving that a higher pitch angle implies that more lift is produced

- Data about launch conditions (throw speed and initial RPM) and flight diameter was collected

1.3 Thesis outline

This final thesis work has the aim of expanding standard boomerangs' capabilities and understanding the features of the Smart Boomerang technology.
The main focus of the work is the dynamical modeling of boomerangs' motion and their position and attitude control. By implementing the motion equation in MATLAB and numerically solving them, it is possible to study the trajectory of the boomerang, and understand the influence of its design, throwing conditions, external conditions, and effects of controllers through different approaches.
The thesis is structured to follow the chronological order in which various tasks were carried out during the internship at NASA JPL.
Chapter 1 introduced the concept of Smart Boomerang, the previous work done on this innovative type of aircraft, and the thesis objectives.
Chapter 2 presents the prototyping process of a Smart Boomerang and the results of experimental tests.
Chapter 3 presents the fundamental quantities needed to analyze the boomerang's equations of motion.
Chapter 4 introduces Boomerang's equations of motion, with two approaches presented: both are based on the Blade Element Theory, with the latter introducing the assumption of small angles of attack. The results will be validated thanks to experimental tests carried out by the Summer Interns.
Chapter 5 will focus on the control features of the probe, exploring its capabilities of trajectory and attitude control with the use of PID controllers.
In Chapter 6, some considerations about the problem of state estimation will be presented, supported by preliminary analyses.
Finally, chapter 7 will summarize the work done and draw conclusions about the project.

Chapter 2

Prototyping and testing

This chapter presents the work done during the first part of the internship carried out at NASA JPL.
The idea is to build a Boomerang which, with the input of a Radio Control signal, can rotate its wings. The objective is to prove that, after being hand-thrown, the wing rotation would imply a shift from the natural Boomerang's trajectory.
The following sections will introduce the design of the Smart Boomerang that was built, and the results of the relative experimental tests that were performed.

2.1 Additive Manufacturing

Additive Manufacturing is the go-to technique for the prototyping of innovative crafts. Its versatility and low cost allow for the design and Fast Prototyping of numerous parts. The main technique used was the Fusion Deposition Modeling (FDM) with commercially available 3D-Printers: a nozzle deposits layers of a fused polymeric compound on a bed, and the desired component is printed layer-by-layer.
Different materials can be used for 3D printing. Table 2.1 summarizes the most commonly used materials and their Young Modulus and Density properties. Poly-lactic acid (PLA) was chosen for the production of the Smart Boomerang prototypes: while ABS presents a beneficial lower density which would be helpful to build a lighter and therefore more maneuverable aircraft, it also presents a lower Young Modulus, making the PLA a more ideal choice for a Smart Boomerang that has to be thrown and tested multiple times while preserving shape and integrity.

Polymer	**Young Modulus [MPa]**	**Density** $[kg7m^3]$
ABS	2100	1.05
PLA	3500	1.25
TPU	from 10 to 1000	1.23

Table 2.1: Polymers used for 3D printing

2.2 Smart Boomerang design overview

The Smart Boomerang design is an evolution of the proposed design developed by the Summer 2023 Interns (fig. 1.7). As shown in figure 2.1, the Smart Boomerang is externally made by an Electronics Hub, which is connected through a threaded rod to the Boomerang's wings.
The Electronic Hub is made up of two half shells which can be joined together with nuts and screws.
The Electronic Hub contains the electronics and the mechanism through which the rotation of the wings is performed (fig. 2.2). A servo motor is coupled with a 3D-printed main bevel gear. Each wing is connected to another 3D-printed small bevel gear, so that when the servo motor rotates, the main gear spins with it, and all of the small gears follow its motion collectively rotating all of the boomerang's wings.
The wings are printed with a NACA 0012 airfoil and are slightly larger towards the tip. The wing's root and tip are flat, allowing the component to be 3D printed without any supports. The root section is about 2 cm wide while the largest is 4 cm wide, with the blade length being 18 cm. These proportions are empirically found to be suited for a well-crafted Boomerang in [10].
Heat inserts are put inside the wings and small gears to connect them through the threaded rod; plastic standoffs are applied to further increase the stiffness of the rod and avoid its bending under stresses that can occur at impact.

2.2.1 Electronic components

The electronic components used for the Smart Boomerang are represented in figure 2.3. All of the equipment is commercially available and it consists of:

- A 250 mAH Battery with a nominal potential difference of 3.7 V (full charge: 4.2 V)

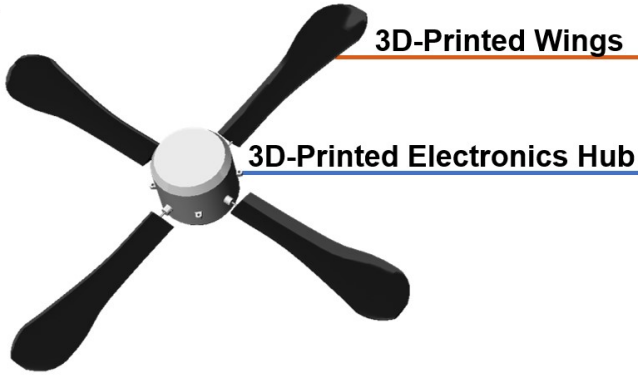

Figure 2.1: Smart Boomerang design

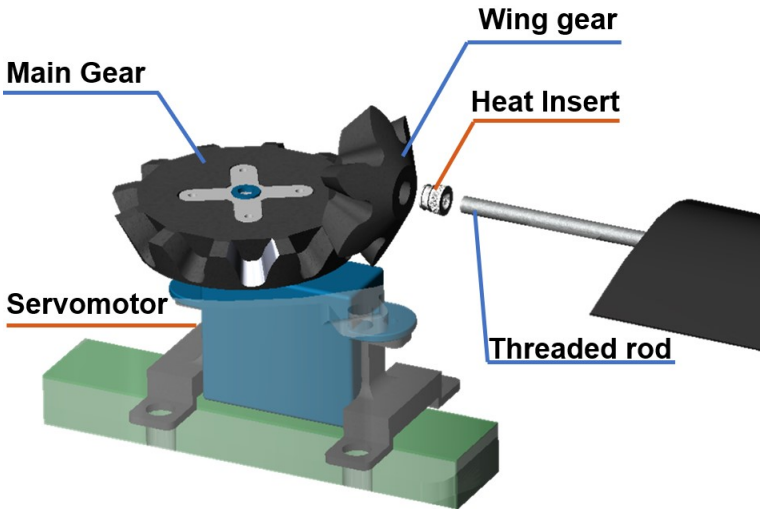

Figure 2.2: Wing rotation mechanism

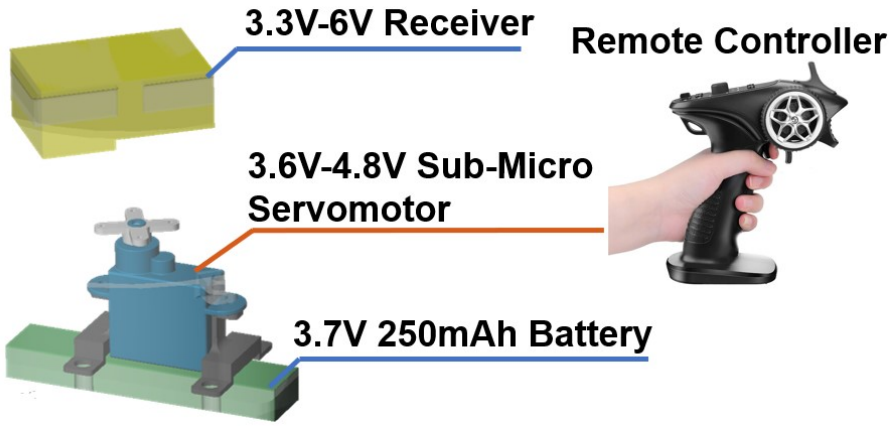

Figure 2.3: Electronic equipment

- A sub-micro servo motor capable of operating at potential differences between 3.6 and 4.8 V
- A receiver capable of operating at potential differences between 3.3 and 6.6 V
- An external Radio Controller, which is needed to operate the boomerang

It was essential to select components whose functioning range included the operative voltage supported by the battery, to avoid the use of components like amplifiers or BECs which would end up increasing the weight and complexity of the Boomerang.

2.3 Experimental tests

Many experimental tests were run, using Smart Boomerang configurations with three or four wings. The former weighed about 180 grams, the latter 210 grams. The experimental setup was composed of a camera to record the Boomerang's trajectory, with marks used to measure the distance traveled.
An example of a trajectory obtained in an experimental test is reported in figure 2.4. It can be seen that the trajectory is a parabola. This means that the boomerang was producing little to no lift, being unable to fly back to the thrower or perform any trajectory control maneuver.
The problem with the experimental tests was that, given the large diameter of the boomerang disk (about half a meter) and its weight, the large moment of

Figure 2.4: Experimental test - boomerang trajectory reported in white

inertia made it difficult to throw the aircraft by hand. Average throw speeds were less than 18 m/s, with about 2 revolutions completed for every second of flight. Boomerangs are usually thrown at speeds of 20 m/s or above and with a rotational speed of over 8 revolutions per second. The Smart Boomerang prototype proved to be nearly impossible to work when thrown at such translational and rotational speeds. This left three options about how to proceed with the thesis work:

1. Practice throwing until a returning trajectory is achieved
2. Fix and improve the Launcher developed by the Summer Interns and use it for the tests
3. Develop a tool for virtual testing

Given the limited time available and the fact that a one-man group worked on the project, option 3 was chosen, as it allows the gathering of large amounts of data in a time- and cost-effective manner.

Chapter 3

Fundamental quantities

This chapter introduces the basics for studying a moving and rotating object, like a boomerang, inside an inertial space.

3.1 Transport Theorem

The study of boomerang dynamics requires using different inertial frames, which will be described in detail in the following chapters. However, it is useful to introduce here the Transport Theorem [1], which allows us to relate the derivative of a vector $\vec{f}$ in an inertial frame to the derivative of the same vector in a rotating body-fixed frame:

$$\left(\frac{d\vec{f}}{dt}\right)_I = \left(\frac{d\vec{f}}{dt}\right)_b + \vec{\omega}_{b/I} \times \vec{f} \tag{3.1}$$

where the subscripts I and b indicate that the quantities are related respectively to the inertial and body frames, $\vec{\omega}_{b/I}$ is the relative angular velocity between the body frame and the inertial frame (which, considering that the inertial frame is fixed in space, corresponds to the angular velocity of the body frame) represented in the body-frame, and $\vec{\omega}_{b/I} \times \vec{f}$ is the vector product between the two quantities.

3.2 Euler Angles and reference systems

Euler angles represent a body's attitude, presenting the advantage of being easy to interpret with respect to other methods like quaternions, which will be introduced in the next section. The idea is that it is possible to overlap two orthogonal frames using three rotations of one of them around its reference axes. Figure 3.1 shows a so-called 3-2-1 rotation where an inertial reference system (X_I, Y_I, Z_I) is rotated

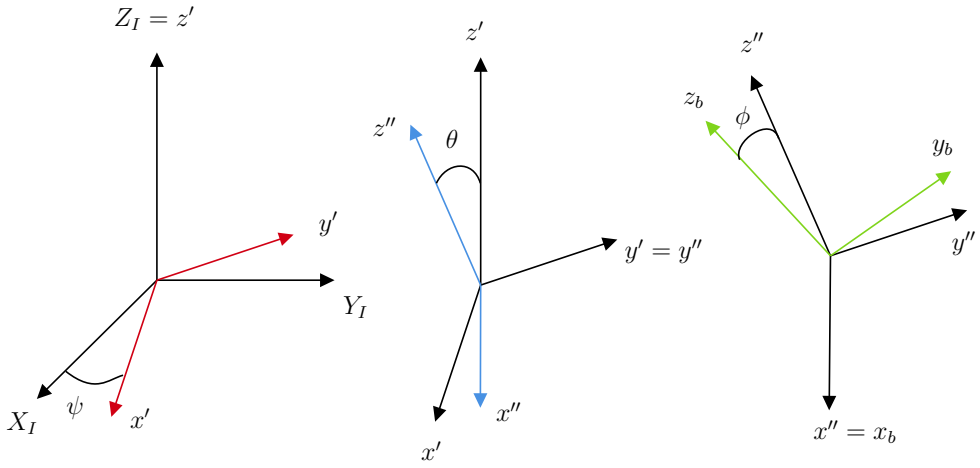

Figure 3.1: Euler Angles - 3-2-1 rotation

to overlap the body system (x_b, y_b, z_b). First, the inertial frame is rotated about its Z_I axis by a yawing angle ψ. A second rotation of a pitching angle θ about the y' axis follows. Finally, a rotation of rolling angle ϕ about the x'' axis aligns the inertial frame with the body one.
The rotation matrices that describe the transformation are:

$$\begin{aligned} R_3(\psi) &= \begin{bmatrix} \cos\psi & \sin\psi & 0 \\ -\sin\psi & \cos\psi & 0 \\ 0 & 0 & 1 \end{bmatrix} \\ R_2(\theta) &= \begin{bmatrix} \cos\theta & 0 & -\sin\theta \\ 0 & 1 & 0 \\ \sin\theta & 0 & \cos\theta \end{bmatrix} \\ R_1(\phi) &= \begin{bmatrix} 1 & 0 & 0 \\ 0 & \cos\phi & \sin\phi \\ 0 & -\sin\phi & \cos\phi \end{bmatrix} \end{aligned} \tag{3.2}$$

The matrix that transforms the inertial frame into the body frame is defined as $T_0 = R_1(\psi)R_2(\theta)R_3(\phi)$. The detailed expression for the matrix is:

$$T_0 = \begin{bmatrix} c(\psi)c(\theta) & c(\theta)s(\psi) & -s(\theta) \\ c(\psi)s(\phi)s(\theta) - c(\phi)s(\psi) & c(\phi)c(\psi) + s(\phi)s(\psi)s(\theta) & c(\theta)s(\phi) \\ s(\phi)s(\psi) + c(\phi)c(\psi)s(\theta) & c(\phi)s(\psi)s(\theta) - c(\psi)s(\phi) & c(\phi)c(\theta) \end{bmatrix} \tag{3.3}$$

Where c and s have been used to represent cos and sin in a short form.
The matrix T_0, like all rotation matrices, is orthonormal, thus it respects the

following property:

$$T_0 T_0^T = I_{3x3},\ det(T_0) = 1$$

3.2.1 Angular velocity and Euler Angle rates

A relationship between the rate of change of the Euler Angles of the 3-2-1 rotation and the angular velocity can be established:

$$\vec{\omega}_{b/I} = [p\ q\ r]^T = \dot{\psi}\hat{Z}_I + \dot{\theta}\hat{y'} + \dot{\phi}\hat{x_b}$$

where the hat notation represents that the unit vector is being considered and the dot above a variable represents its derivative with respect to time. By using the rotation matrices defined in equations 3.2, the angular velocity can be represented in body coordinates as:

$$\vec{\omega}_{b/I} = [p\ q\ r]^T = \dot{\psi}R_1R_2\hat{z_b} + \dot{\theta}R_1\hat{y_b} + \dot{\phi}\hat{x_b}$$

In explicit form, we have:

$$\begin{aligned} p &= \dot{\phi} - \dot{\psi}\sin\theta \\ q &= \dot{\theta}\cos\phi + \dot{\psi}\cos\theta\sin\phi \\ r &= -\dot{\theta}\sin\phi + \dot{\psi}\cos\phi\cos\theta \end{aligned} \tag{3.4}$$

Thus, we can now define the rate of change of the Euler Angles as a function of the angular velocity:

$$\begin{aligned} \dot{\phi} &= p + q\sin\phi\tan\theta + r\cos\phi\tan\theta \\ \dot{\theta} &= q\cos\phi - r\sin\phi \\ \dot{\psi} &= q\frac{\sin\phi}{\cos\theta} + r\frac{\cos\phi}{\cos\theta} \end{aligned}$$

This set of equations can be written in matrix form:

$$\begin{Bmatrix} \dot{\phi} \\ \dot{\theta} \\ \dot{\psi} \end{Bmatrix} = \begin{bmatrix} 1 & \sin(\phi)\tan(\theta) & \cos(\phi)\tan(\theta) \\ 0 & \cos(\phi) & -\sin(\phi) \\ 0 & \frac{\sin(\phi)}{\cos(\theta)} & \frac{\cos(\phi)}{\cos(\theta)} \end{bmatrix} \begin{Bmatrix} p \\ q \\ r \end{Bmatrix} = A\vec{\omega} \tag{3.5}$$

Equation 3.5 can be used to update Euler Angles, and therefore the attitude of the analyzed body, during its motion. However, we can note that as the pitching angle approaches values close to $\theta = \pm\frac{\pi}{2}$, the rates of change for roll and yaw angles tend to infinity.

For this reason, Euler Angles will be used in this work for the scope of intuitively understanding the attitude kinematics of the boomerang during its flight. However, computation of its attitude will be performed employing quaternions.

3.3 Quaternions

Quaternions allow the alignment of two orthonormal frames with a single rotation. The idea is based upon the *Euler's eigenaxis rotation theorem*: *it is possible to rotate a fixed frame F_I onto any arbitrary frame F_B with a simple rotation around an axis $\hat{a}$ that is fixed in both frames, called the Euler's rotation axis or eigenaxis. [2].* The Euler Angle is defined as the rotation angle around the Euler Axis $\hat{a}$ Let us call α the Euler Angle, and $[e_1\ e_2\ e_3]$ the components of $\hat{a}$. A quaternion presents four components: $\vec{q} = [q_0\ q_1\ q_2\ q_3\ ]^T$, each defined as:

$$q_0 = \cos\frac{\alpha}{2}$$
$$q_1 = e_1 \sin\frac{\alpha}{2}$$
$$q_2 = e_2 \sin\frac{\alpha}{2}$$
$$q_3 = e_3 \sin\frac{\alpha}{2}$$

A property of every quaternion is:

$$q_0^2 + q_1^2 + q_2^2 + q_3^2 = 1$$

A quaternion defines an object's attitude with reference to an inertial frame, and its evolution presents no singularity.
We can define its evolution as [2]:

$$\begin{Bmatrix} \dot{q_0} \\ \dot{q_1} \\ \dot{q_2} \\ \dot{q_3} \end{Bmatrix} = \frac{1}{2} \begin{bmatrix} 0 & -p & -q & -r \\ p & 0 & r & -q \\ q & -r & 0 & p \\ r & q & -p & 0 \end{bmatrix} \begin{Bmatrix} q_0 \\ q_1 \\ q_2 \\ q_3 \end{Bmatrix}$$

or, in matrix form:

$$\dot{\vec{q}} = Q\vec{q} \tag{3.6}$$

by distinguishing between the quaternion's scalar part q_0 and its vectorial part $\vec{q_v} = [q_1\ q_2\ q_3\ ]^T$, we can rewrite equation 3.6 as:

$$q_0 = -\frac{1}{2}\vec{\omega} \cdot \vec{q} \tag{3.7}$$

$$\vec{q_v} = \frac{1}{2}(q_0\vec{\omega} - \vec{\omega} \times \vec{q}) \tag{3.8}$$

From a quaternion, we can also obtain the equivalent rotation matrix:

$$R = \begin{bmatrix} q_0^2 + q_1^2 - q_2^2 - q_3^2 & 2(q_1q_2 + q_0q_3) & 2(q_1q_3 - q_0q_2) \\ 2(q_1q_2 - q_0q_3) & q_0^2 - q_1^2 + q_2^2 - q_3^2 & 2(q_2q_3 + q_0q_1) \\ 2(q_1q_3 + q_0q_2) & 2(q_2q_3 - q_0q_1) & q_0^2 - q_1^2 - q_2^2 + q_3^2 \end{bmatrix}$$

Chapter 4

Dynamical Modeling

This chapter describes the equation of motion for boomerangs. The aerodynamic forces and moments will be modeled using the Blade Element Theory [3]. The effect of throwing conditions and wind will be thoroughly studied and presented, while also being compared with results from previously published papers [3], [4]. Two models will be presented, with the latter introducing the assumption of small angles of attack [12].

4.1 Reference systems

Four reference systems are useful to describe the equations of motion of the boomerang:

1. (X_I, Y_I, Z_I) An inertial reference system, identified by East-North-Up coordinates (ENU) and centered on the thrower, needed to study the boomerang's trajectory

2. (x_b, y_b, z_b) A body-fixed system, with its origin fixed to the body center of mass, needed to study the forces and moments acting on the boomerang in the body frame

3. (ξ, η, ζ) A wing reference system, with its second axis η aligned with the aerodynamic center of the wings (assuming a constant wing section), useful for the computation of aerodynamic forces and torques

4. (x_n, y_n, z_n) A non-spinning body-fixed frame, which allows to study the attitude of the boomerang

The transformation from the inertial frame to the body frame is carried out using the rotation matrix T_0 defined in equation 3.2.
To obtain the wing frame, it is necessary to move the origin of the body frame from the Center of Mass to the aerodynamic center of the wing. This distance is identified by the quantity $r_{ac,j}$. After doing this, the following three rotations are performed [3]:

1. Rotation of $\Lambda_j - pi/2$ around the z_1 axis
2. Rotation of β_j around the x_2 axis
3. Rotation of θ_j around the $y_3 \equiv \eta$ axis

where Λ is the wing's sweep angle, β is its flapping angle, θ the wing pitch and the subscript j indicates that the $j-th$ wing is being considered. The process for obtaining the wing frame is illustrated in Fig. 4.1. The following matrices describe the rotation:

$$R_{3j} = \begin{bmatrix} \cos(\Lambda_j - \frac{\pi}{2}) & \sin(\Lambda_j - \frac{\pi}{2}) & 0 \\ -\sin(\Lambda_j - \frac{\pi}{2}) & \cos(\Lambda_j - \frac{\pi}{2}) & 0 \\ 0 & 0 & 1 \end{bmatrix} \tag{4.1}$$

$$R_{1j} = \begin{bmatrix} 1 & 0 & 0 \\ 0 & \cos(\beta_j) & \sin(\beta_j) \\ 0 & -\sin(\beta_j) & \cos(\beta_j) \end{bmatrix} \tag{4.2}$$

$$R_{2j} = \begin{bmatrix} \cos(\theta_j) & 0 & -\sin(\theta_j) \\ 0 & 1 & 0 \\ \sin(\theta_j) & 0 & \cos(\theta_j) \end{bmatrix} \tag{4.3}$$

It is useful to define the joint angle γ, which represents the angle between two consecutive wings. Thus we have:

$$\Lambda_{j+1} = \Lambda_j + \gamma$$

The final rotation matrix that allows to transform the shifted body-fixed frame in the wing frame is:

$$T_j = \begin{bmatrix} s(\Lambda_j)c(\theta_j) + c(\Lambda_j)s(\beta_j)s(\theta_j) & s(\Lambda_j)s(\beta_j)s(\theta_j) - c(\Lambda_j)c(\theta_j) & -c(\beta_j)s(\theta_j) \\ c(\Lambda_j)c(\beta_j) & s(\Lambda_j)c(\beta_j) & s(\beta_j) \\ s(\Lambda_j)s(\theta_j) - c(\Lambda_j)s(\beta_j)c(\theta_j) & -c(\Lambda_j)s(\theta_j) - s(\Lambda_j)s(\beta_j)c(\theta_j) & c(\beta_j)c(\theta_j) \end{bmatrix} \tag{4.4}$$

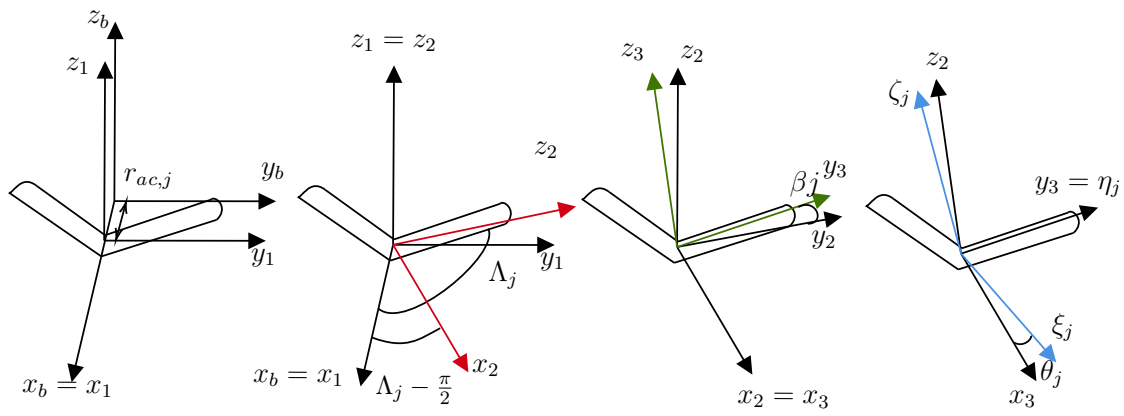

Figure 4.1: Steps to rotate the body-fixed frame into the wing frame

Finally, the non-spinning frame is obtained from the body-fixed frame by considering the angle λ, where [3]:

$$\lambda = \int_0^t (r - r_n)dt = -\tan^{-1}\left(\frac{u_y}{u_x}\right) \tag{4.5}$$

where r and r_n are the angular rates around the z_b axis respectively of the body-fixed and non-spinning frame, and u_x, u_y are the velocities of the boomerang's Center of Mass in body coordinates. The non-spinning frame can therefore be obtained from the body-fixed one through the following rotation matrix:

$$T_n = \begin{bmatrix} \cos(\lambda) & -\sin(\lambda) & 0 \\ \sin(\lambda) & \cos(\lambda) & 0 \\ 0 & 0 & 1 \end{bmatrix} \tag{4.6}$$

The transformation matrix from the inertial frame to the non-spinning one is given by $T = T_n T_0$. Thus, the Euler Angles Φ, Θ, and Ψ can be obtained and used to describe the attitude of the non-spinning frame.

4.2 Equations of motion

The derivation of the equations of motion is based on the definition of the forces and moments acting on the boomerang. Throughout the study, the following assumptions will be considered valid:

- The boomerang is a rigid body

- The aerodynamic forces and moments can be computed using the Blade Element Theory (BET)
- The aerodynamic coefficients used in the BET have negligible variation within the range of Reynolds at which the boomerang flies
- The boomerang's center of mass is aligned with its rotation axis

First of all, recalling the transport theorem from equation 3.1, we can recall Newton's second law and its equivalent for rotation:

$$\sum \vec{F} = \vec{F}^I = \left(\frac{d(m\vec{V})}{dt}\right)_I = \left(\frac{d(m\vec{v})}{dt}\right)_b + m\vec{\omega}_{b/I} \times \vec{v} = m\left(\dot{\vec{v}} + \vec{\omega}_{b/I} \times \vec{v}\right) \quad (4.7)$$

$$\sum \vec{M} = \vec{M}^I = \left(\frac{d(I\vec{\Omega})}{dt}\right)_I = \left(\frac{d(I\omega)}{dt}\right)_b + \vec{\omega}_{b/I} \times I\vec{\omega} = I\dot{\vec{\omega}} + \vec{\omega}_{b/I} \times I\vec{\omega} \quad (4.8)$$

where m is the boomerang's mass, I its moment of inertia, V and Ω are the velocity and angular velocity measured in the inertial frame, v and ω are the velocity and angular velocity measured in the body frame. Since $\vec{\omega}_{b/I} = \vec{\omega}$, the subscript will be dropped from now on for simplicity of notation. Equations 4.7 and 4.8 can be rewritten as:

$$\begin{aligned} F_1^I &= m\left(\dot{v}_1 + qv_3 - rv_2\right) \\ F_2^I &= m\left(\dot{v}_2 + rv_1 - pv_3\right) \\ F_2^I &= m\left(\dot{v}_3 + pv_3 - rv_1\right) \end{aligned} \quad (4.9)$$

$$\begin{aligned} M_1^I &= I\dot{p} + (I_3 - I_2)qr \\ M_2^I &= I\dot{q} + (I_1 - I_3)pr \\ M_1^I &= I\dot{r} + (I_2 - I_1)pq \end{aligned} \quad (4.10)$$

where equation 4.10 has been written assuming a diagonal inertia matrix, which is a good approximation considering that boomerangs usually present a plane of symmetry. The main forces acting on the boomerang are the aerodynamic and gravitational ones. Considering the body-fixed frame, and assuming that the Center of Mass coincides with the Instantaneous Center of Rotation, the only moment acting on the boomerang is the aerodynamic one:

$$\begin{cases} F^A + F^G = F^I \\ M^A = M^I \end{cases} \quad (4.11)$$

Aerodynamic forces and moments will be derived in the section regarding the Blade Element Theory. The gravity force is rotated in the body frame so that we have that:

$$F^G = -mgT_0\hat{K}_I = -mgT_0[0\ 0\ 1]^T \tag{4.12}$$

Finally, we can write a system of nine equations that describe the boomerang's motion:

$$\begin{cases} \dot{\vec{v}} = \frac{1}{m}\left(\vec{F}^A + \vec{F}^G - \vec{\omega} \times \vec{v}\right) \\ [\dot{\phi}\ \dot{\theta}\ \dot{\psi}]^T = A\vec{\omega} \\ \dot{\vec{\omega}} = I^{-1}\left(\vec{M}^A - \vec{\omega} \times I\vec{\omega}\right) \end{cases} \tag{4.13}$$

Which can be alternatively written using quaternions in place of Euler Angles:

$$\begin{cases} \dot{\vec{v}} = \frac{1}{m}\left(\vec{F}^A + \vec{F}^G - \vec{\omega} \times \vec{v}\right) \\ \dot{\vec{q}} = Q\vec{q} \\ \dot{\vec{\omega}} = I^{-1}\left(\vec{M}^A - \vec{\omega} \times I\vec{\omega}\right) \end{cases} \tag{4.14}$$

4.2.1 Blade Element Theory

The Blade Element Theory is the state-of-the-art method for most analyses regarding helicopter rotor aerodynamics. Considering that a boomerang can be considered as a rotor with a very high advance ratio $\mu = \frac{v}{\omega R}$ (with R being the radius of rotation of the spinning boomerang disk), this theory works well to estimate the aerodynamic forces and moments acting on this special type of aircraft. The idea of Blade Element Theory is to discretize a blade as a series of quasi-2D airfoil sections, compute the aerodynamic forces and moments acting on each section, and then integrate the quantities over the wingspan's length [8]. We can therefore write the formulas for the incremental lift and drag acting on a section of the wingspan:

$$\begin{aligned} dL &= \frac{1}{2}\rho w^2 c C_L(\alpha) d\eta \\ dD &= \frac{1}{2}\rho w^2 c C_d(\alpha) d\eta \end{aligned} \tag{4.15}$$

where ρ is the air density, w is the relative velocity in wing-system coordinates, c is the mean chord of the wing section, C_L, and C_D are the coefficients of lift and

drag specific to the chosen airfoil Let l, d and m be defined as:

$$\begin{aligned} l &= \frac{1}{2}\rho w^2 c C_L(\alpha) \\ d &= \frac{1}{2}\rho w^2 c C_D(\alpha) \\ m &= \frac{1}{2}\rho w^2 c^2 C_M(\alpha) \end{aligned} \tag{4.16}$$

with m being the pitching moment per unit of wingspan and C_M the coefficient of the pitching moment. The relative air velocity w is given by the sum of the translational and rotational velocities:

$$w = T_j \left(-\vec{v} - \vec{\omega} \times \vec{r} + \vec{v}_i\right) \tag{4.17}$$

where $\vec{v}_i$ is the induced velocity at the rotor disk, which will be derived in the following section.
With the help of figure 4.2, we can write the equations that define the forces and moments acting on the wing section:

$$\begin{aligned} F^A_{1,j} &= \int_{l_r}^{l_t} \left(-l \sin\alpha + d\cos\alpha\right) d\eta \\ F^A_{2,j} &= 0 \\ F^A_{3,j} &= \int_{l_r}^{l_t} \left(l\cos\alpha + d\sin\alpha\right) d\eta \end{aligned} \tag{4.18}$$

where $\alpha = tan^{-1}\left(\frac{w_3}{w_1}\right) * \theta_j$ is the Angle of Attack (AoA). The aerodynamic moments will be:

$$\begin{aligned} M^A_{1,j} &= \int_{l_r}^{l_t} dF^A_{3,j}\eta d\eta \\ M^A_{2,j} &= \int_{l_r}^{l_t} m d\eta \\ M^A_{3,j} &= \int_{l_r}^{l_t} -dF^A_{1,j}\eta d\eta \end{aligned} \tag{4.19}$$

where the integration is computed from the position of the wing root l_r to the position of the wing tip l_t. The assumption made is that the velocity component over the wing span has a negligible aerodynamic effect on the dynamics.
Finally, the total aerodynamic forces and moments acting on the boomerang will be given by the sum of the ones acting on each wing, and rotated through the

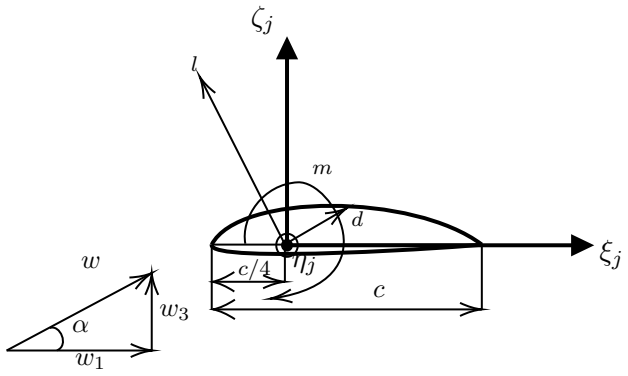

Figure 4.2: Forces and moments acting on the 2D section

rotation matrix T_j^{-1} to represent the quantities in body-frame coordinates:

$$\begin{aligned} F^A &= \sum_{i=1}^{n_w} T_j^{-1} F_j^A \\ M^A &= \sum_{i=1}^{n_w} (T_j^{-1}(M_j^A + r_{ac,j} \times F_j^A)) \end{aligned} \tag{4.20}$$

where n_w represents the number of wings.

Induced velocity

The rotating blades impart a so-called induced velocity at the rotor disk. From the Momentum Theory Analysis, it is possible to derive an equation that describes the induced velocity for hovering flight [8]:

$$\bar{v}_{ih} = \sqrt{\frac{F_3^A}{2\rho S}}$$

with S being the surface area of the rotor disk. For analysis in forward flight, the formula becomes:

$$\bar{v}_i = \frac{\bar{v}_{ih}^2}{\sqrt{v_t^2 + (v_3 + \bar{v}_i)^2}} \tag{4.21}$$

where v_t is the velocity tangential to the rotor disk and v_3 is the perpendicular one. Equation 4.21 can be solved iteratively with a fixed-point or Newton method, or using MATLAB routines like fzero. The equation assumes that the induced velocity is uniform over the rotor disk.

This model can be further improved considering the experiment performed by Brotherhood and Stewart (1949) [8], which showed that the longitudinal inflow variation is approximately linear. By indicating with $\bar{v}_i 0$ the induced velocity in the uniform case, we can express the new formula for the total induced velocity at the rotor disk as:

$$\bar{v}_i = \bar{v}_{i0}(1 + k_x r_b \cos\lambda) \tag{4.22}$$

with $r_b = \frac{l}{l_{blade}}$ being the adimensional wingspan coordinate. The final induced velocity vector is:

$$\vec{v_i} = \bar{v}_i \hat{k}_b = [0\ 0\ \bar{v}_i] \tag{4.23}$$

Prandtl's Tip-Loss function

The Blade Element Theory considers each blade section as 2D airfoils acting independently. A tip-loss factor can be introduced to account for the formation of a trailing vortex at the wing's tip that decreases the lift produced. Prandtl derived a formula to estimate a Tip-Loss factor F, assuming a large radius of curvature at the wing's tip. This assumption may not be true for boomerangs, which can present a curved edge at the wing tip, but the factor is considered applicable for the analyses carried out in this work. The Tip-Loss factor is defined as [8]:

$$F = \left(\frac{2}{pi}\right) \cos^{-1}\left(e^{-f}\right) \tag{4.24}$$

where f is a function of the number of blades, the wingspan position, and the local angle of attack:

$$f = \frac{n_w}{2}\left(\frac{1 - r_b}{r_b \alpha}\right) \tag{4.25}$$

Figure 4.3 shows the influence of the tip loss factor on a blade.

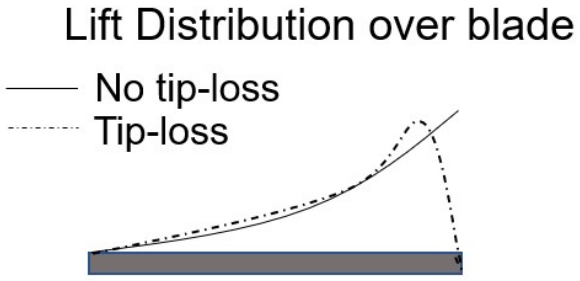

Figure 4.3: Comparison between BET without and with a tip-loss factor

4.3 Validation

One of the experiments run by the Summer Interns is used to validate the developed simulator. Tables 4.1 and 4.2 describe the geometrical and launch parameters of the Boomerang used for the experimental tests.
The same geometrical conditions were considered to model the "virtual" Boomerang within the simulation environment. The considered launch conditions are reported in table 4.3, along with the resulting predicted trajectory parameters. Figure 4.4 shows the trajectory obtained in experimental tests and the one predicted by the simulator.
We can see that the qualitative behavior is quite similar in the first phase of flight: both the experimental and virtual boomerangs start their trajectory in a level flight, after which they start to gain height and return close to the thrower. The experimental boomerang undergoes a steeper fall, followed by a small ascent thanks to the lift produced by the increase of velocity given by the steeper fall. The simulated boomerang comes back close to the thrower in a more gentle fall. In both cases, the final deviation Δx is close to 2 m. The maximum altitude Δz and flight diameter Δy are smaller in the virtual case, with a 5 to 10% difference with reference to the experimental's case lower limit.
The major cause of errors lies in the estimation of the aerodynamic coefficients: as previously stated, the Reynolds number is considered constant at 50.000 Reynolds overall the wingspan, while in reality, it varies much more. The results obtained are still considered valuable and a good prediction of a Boomerang's trajectory. Therefore, the Simulator can reliably be used for preliminary analyses regarding Boomerangs and Smart Boomerangs Missions.

Number of wings	3
Blade length	15.60 cm
Blade chord	3.88 cm
Mass	52 g

Table 4.1: Experimental tests - Boomerang design

Launch speed	$20.9 \pm 3.5m$
Launch RPM	$589 \pm 26m$
Max Δy	15 ± 5 m
Max Δz	5.9 ± 1.7 m
Final deviation	2.3 ± 0.4 m
Flight time	4.7 s

Table 4.2: Experimental tests - Trajectory parameters

Launch speed	23 m/s
Launch RPM	600 RPM
Launch attitude [Φ_0, Θ_0, Ψ_0]	[60, 0, 270] °
Max Δy	9 m
Max Δz	4 m
Final deviation	2 m
Flight time	2.5 s

Table 4.3: Simulation - Launch and trajectory parameters

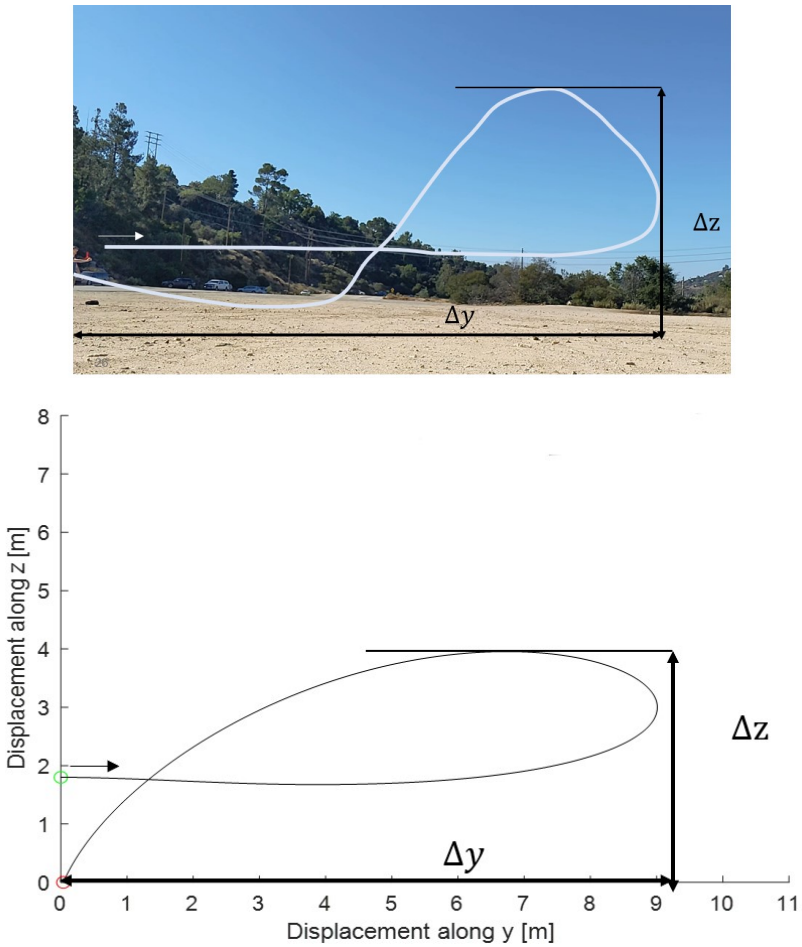

Figure 4.4: Comparison between experimental and simulated trajectories

4.4 Smart Boomerang Prototype Simulation

The objective of this section is to analyze the performance of the Smart Boomerang that was built in Chapter 2, leveraging the developed tool.
The Smart Boomerang prototype had a variable wing chord along the wingspan; for preliminary analysis, it was considered constant and equal to 5 cm. The summary of the geometrical parameters considered for the Smart Boomerang prototype within the simulation is reported in table 4.4.
Figure 4.5 shows how, with a launch speed of about 18 m/s (horizontal velocity: 17 m/s, vertical velocity: 5 m/s) at launch, a parabolic trajectory is obtained.
However, when launching the Boomerang at a speed of 25 m/s and 10 revolutions per second, the returning trajectory shown in figure 4.6 is naturally obtained. Full launch conditions and resulting trajectory parameters are reported in table 4.5 This further proves the need for a dedicated launcher for a Smart Boomerang prototype like the one built.
Figure 4.7 shows the rolling and pitching values during flight: the Boomerang tends to present pitching oscillations, while its rolling angle tends to decrease during flight.
Aerodynamic drag makes the linear and rotational speed decrease during flight, as shown in figure 4.8; however, the Boomerang also undergoes phases where its speed is increasing, which corresponds to times when the Boomerang's vertical lift component is smaller than its weight. Thus, it starts descending to the ground, trading potential energy with kinetic energy; at this time, the aircraft may also enter an autorotation state, thus gaining rotational speed. This the case between 1.1 and 2.3 seconds of flight.

Number of wings	4
Blade length	25 cm
Blade chord	5 cm
Mass	200 g

Table 4.4: Simulation - Smart Boomerang design

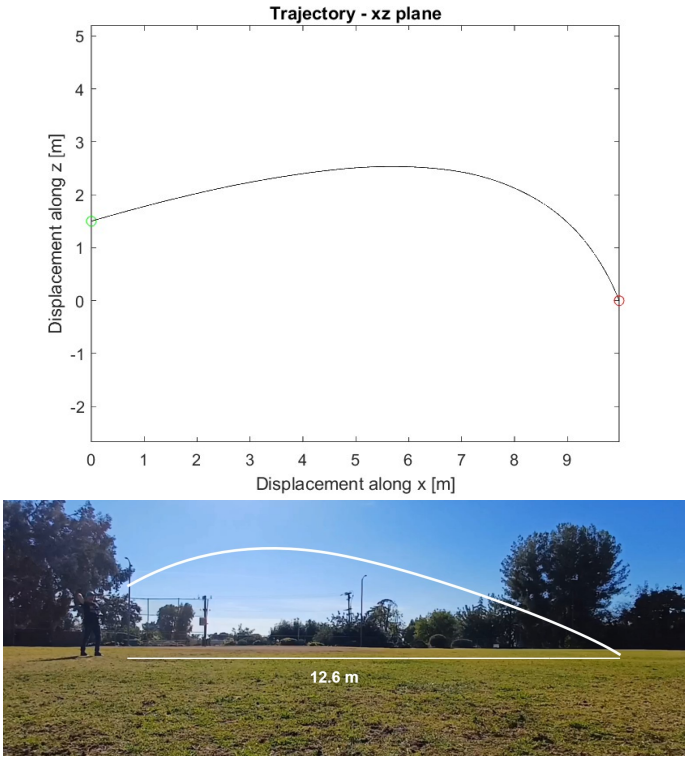

Figure 4.5: Predicted trajectory for the experimental tests run in Chapter 2 compared to the experimental trajectory

Launch speed	25 m/s (Direction: 45° CCW from East)
Launch RPM	600 RPM
Launch attitude $[\Phi_0, \Theta_0, \Psi_0]$	[75, 0, 220] °
Max Δy	12 m
Max Δz	3.5 m
Final deviation	0 m
Flight time	2.85 s

Table 4.5: Simulation - Smart Boomerang design

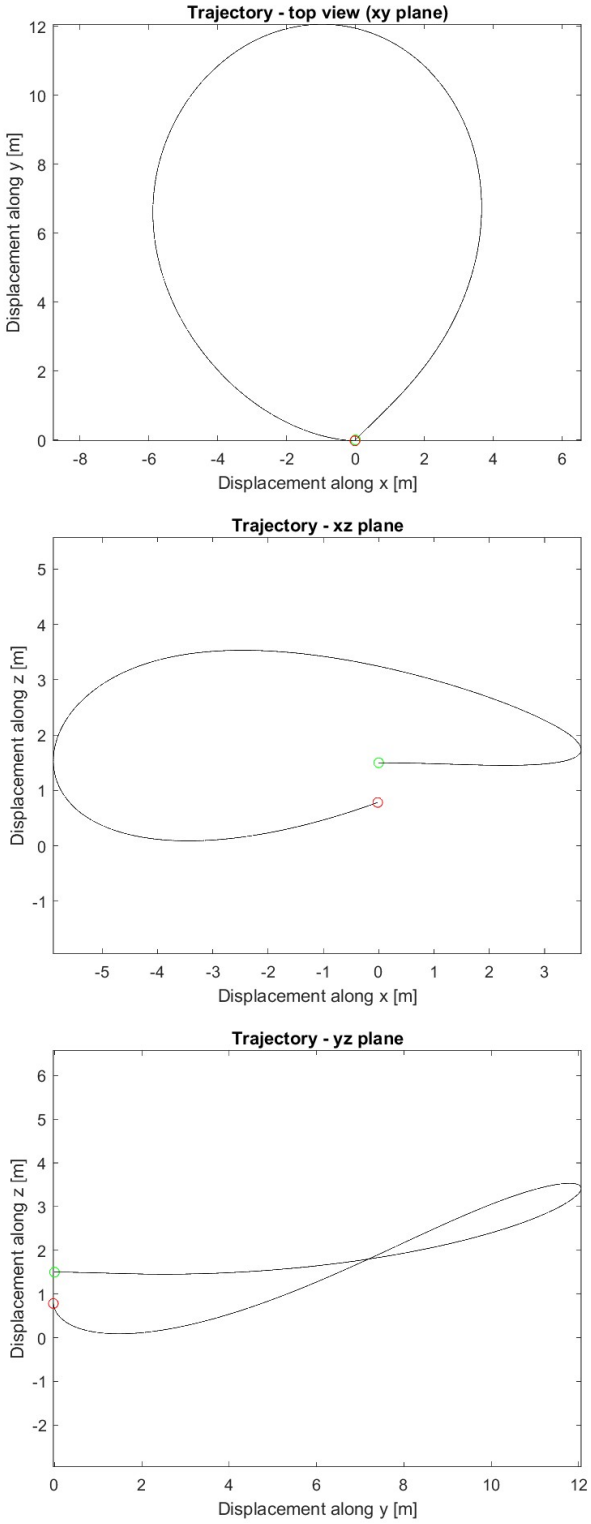

Figure 4.6: Natural returning trajectory of the 4-wings Boomerang

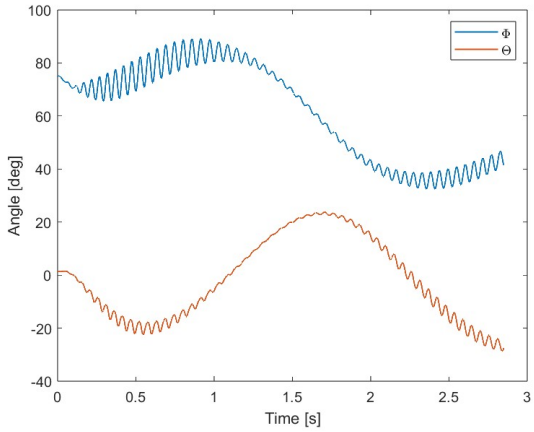

Figure 4.7: Roll angle Φ and pitching angle Θ of the Boomerang during flight

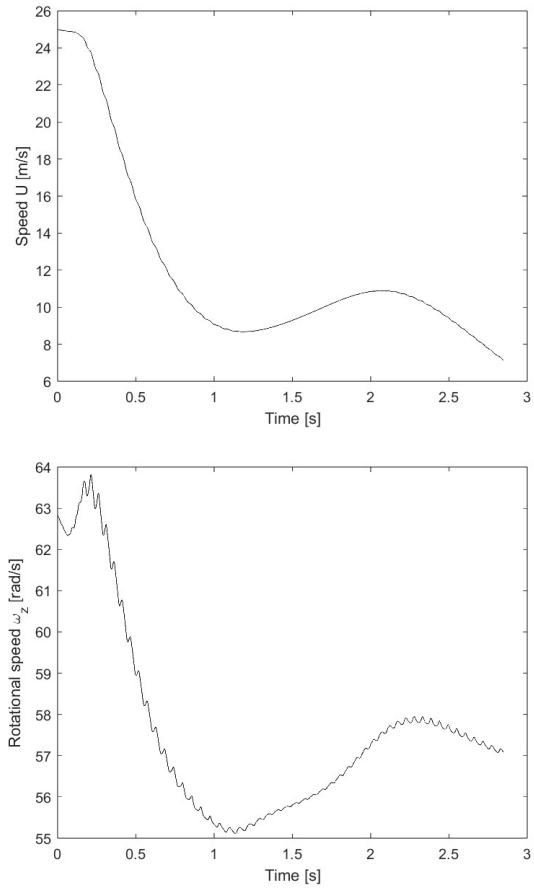

Figure 4.8: Linear and rotational speeds during flight

4.5 Influence of initial conditions and geometry

A Smart Boomerang Mission might require to achieve a wide range of trajectories. While the Boomerangs are planned to be capable of achieving motion control, it is still useful to know how important launch parameters like attitude and speed at launch influence the flight. This would allow to launch of the Boomerang under conditions favorable to complete each specific mission.

4.5.1 Effect of initial roll angle

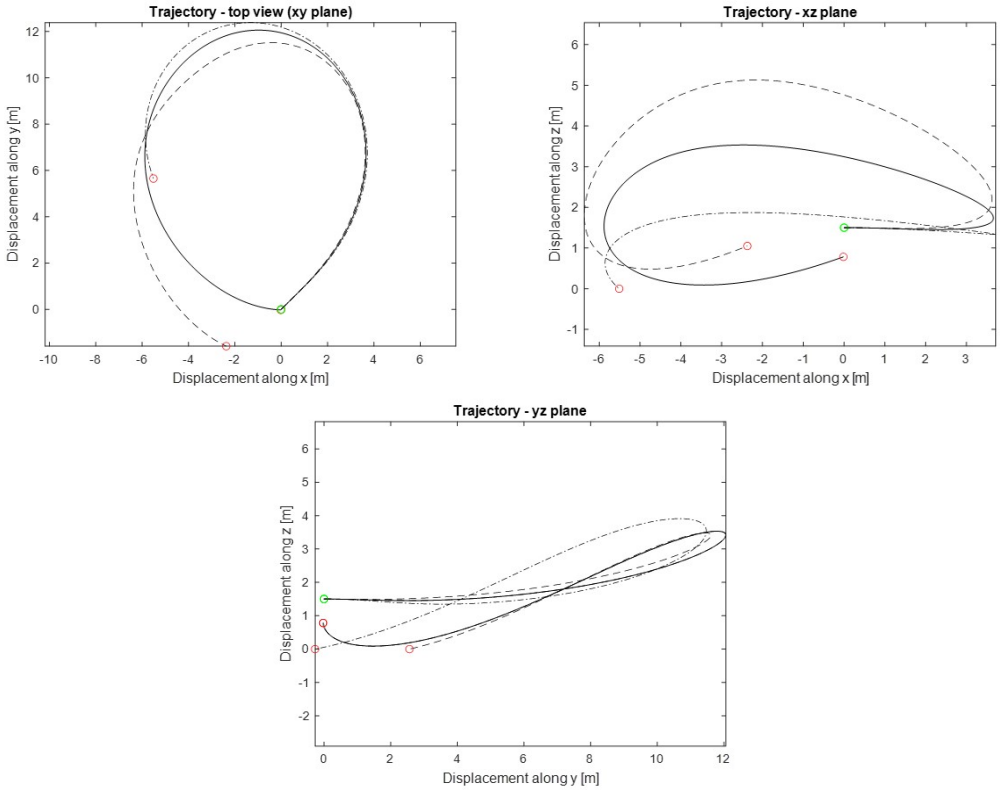

Figure 4.9: —— $\Phi_0 = 75°$, - - - $\Phi_0 = 65°$, -·-·- $\Phi_0 = 85°$

Figure 4.9 shows the effects of decreasing or increasing the roll angle at launch. When the roll angle is decreased, the projection of the Boomerang's lift becomes larger in the Z_I direction and smaller in the centripetal direction. This results in reaching greater heights, while also presenting a larger flight radius, with the aircraft circling behind the thrower.
The opposite effect is seen when increasing the roll angle: the Boomerang produces

a greater component of lift along the centripetal direction, and thus reaches lower heights and falls to the ground in front of the thrower.

4.5.2 Effect of throwing speed

When the Boomerang is thrown at a faster (slower) speed, it reaches a higher (lower) altitude and ends up flying on a smaller (larger) flight radius, as shown in picture 4.10. This effect is given by the increased (decreased) lift that the boomerang produces at higher (lower) flight speeds.

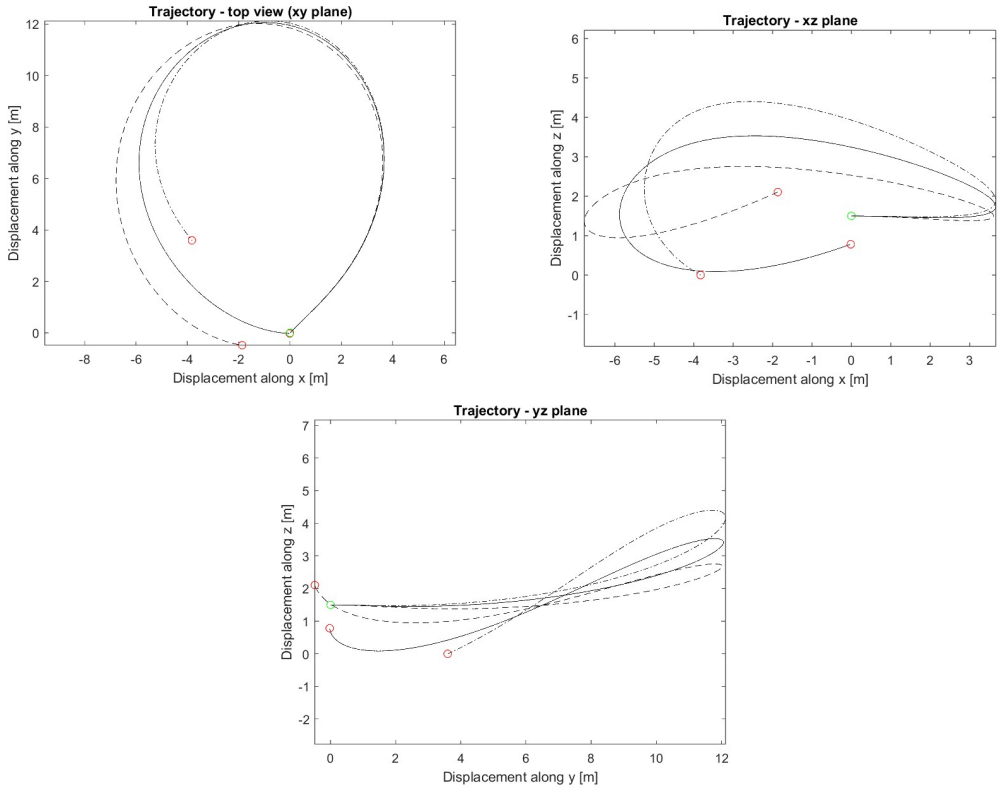

Figure 4.10: —— $U_0 = 25$ m/s, - - - $U_0 = 20$ m/s, -·-·- $U_0 = 30$ m/s

4.5.3 Effect of throw RPM

Throwing the Boomerang at a lower (higher) RPM implies that it will produce less (more) lift as it travels through the air. The effect on the flight radius is not immediately noticeable as in the case of throw speed variation. In this specific case, when the Boomerang is thrown at 12 Hz, it reaches much higher altitudes, momentarily trading off its kinetic energy with potential energy, thus slowing

down and producing less lift, putting it on a larger flight radius in the final part of the trajectory. A dual effect is measured when the RPM is decreased: the Boomerang undergoes a smoother ascent into the air followed by a steeper, fall, making it experience higher velocities and thus produce less lift, resulting in a smaller flight radius in the final part of the trajectory.

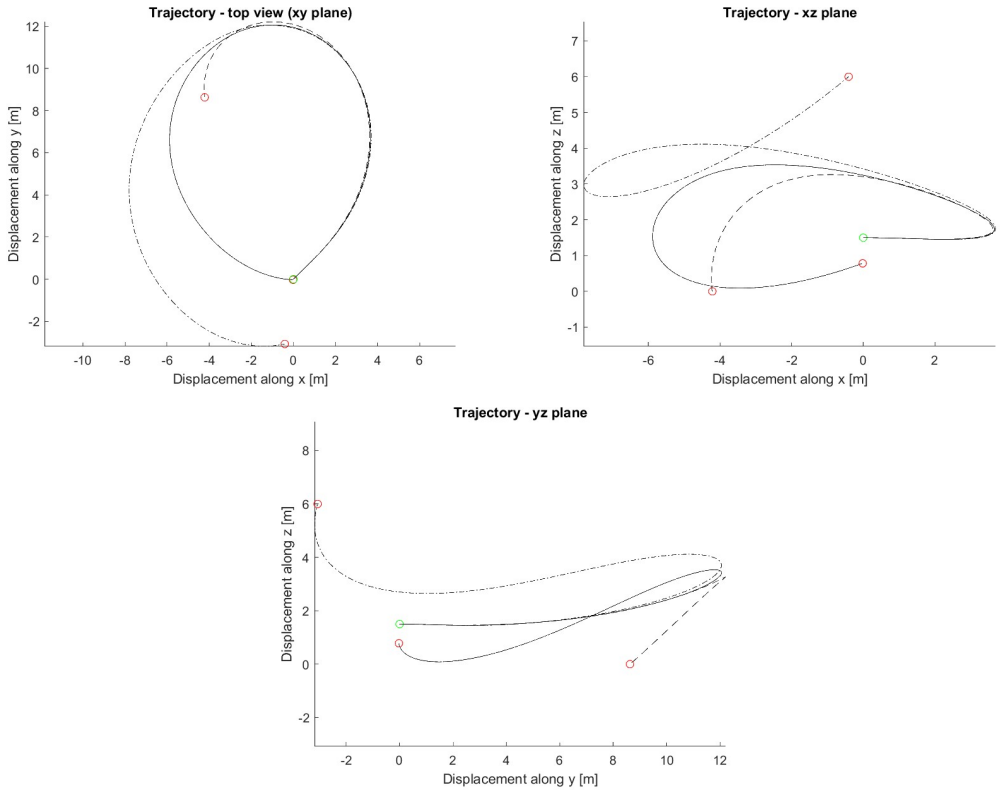

Figure 4.11: —— $\omega_0 = 10$ Hz, - - - $\omega_0 = 8$ Hz, -·-·- $\omega_0 = 12$ Hz

4.5.4 Effect of wing pitch

The effects of wing pitch are reported in figure 4.12. A higher pitch implies a smaller flight radius and higher altitudes: indeed, flying at an increased wing pitch angle means that more lift will be produced during flight. The opposite happens when the wing pitch is decreased, with the boomerang flying on a much larger flight radius, reaching lower altitudes, and falling to the ground after traveling a much shorter path. Producing less lift means that there will be a smaller force counteracting gravity, thus losing valuable flight time.

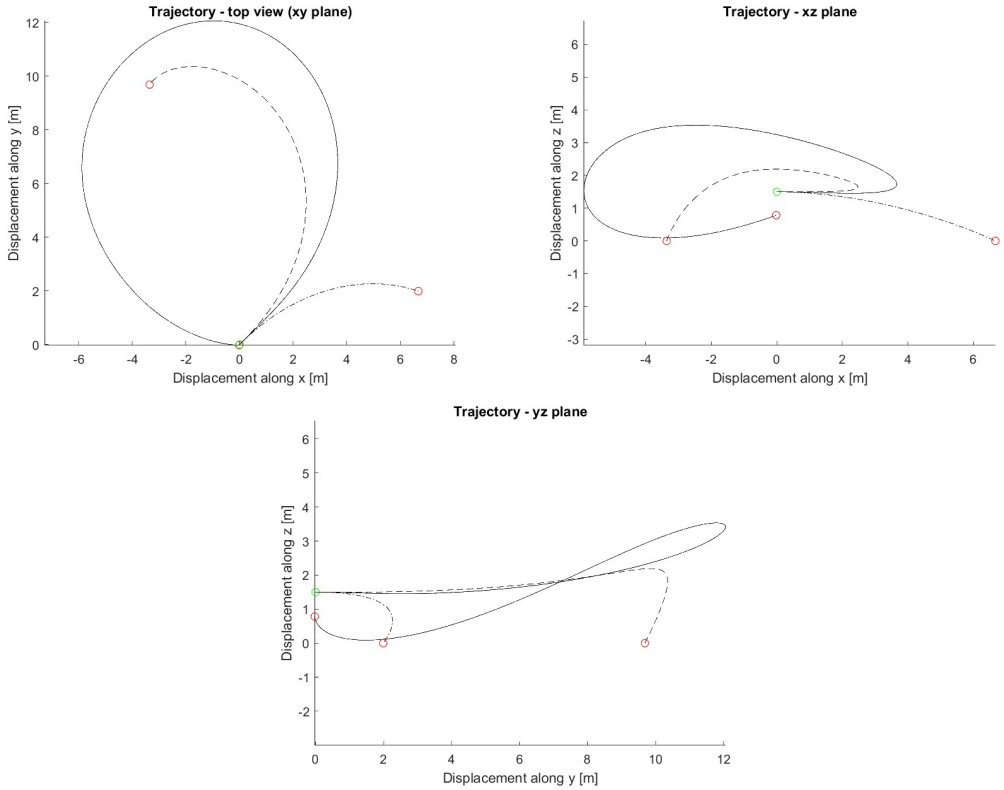

Figure 4.12: —— $\theta = 0°$, - - - $\theta = 5°$, -·-·- $\theta = -5°$

4.5.5 Effect of blade length

Figure 4.13 shows the effects of having shorter or longer wings on flight. A longer (shorter) blade produces more (less) lift. The Boomerang will then initially fly at a smaller (larger) flight radius. Still, as it gains (loses) altitude, its velocity will decrease (increase), with the returning flight phase occurring at a larger (lower) radius.

4.5.6 Effect of dihedral angle

Effects of the wing's dihedral angle on trajectory are represented in figure 4.14. The reference trajectory is obtained with a Boomerang designed to have a dihedral angle of $\beta = 4°$. Decreasing (increasing) this angle results in the Boomerang disk becoming larger (smaller), thus having a similar effect to the one of increasing its wing surface. Therefore, the flight path radius will increase (decrease) and it will reach lower (higher) altitudes.

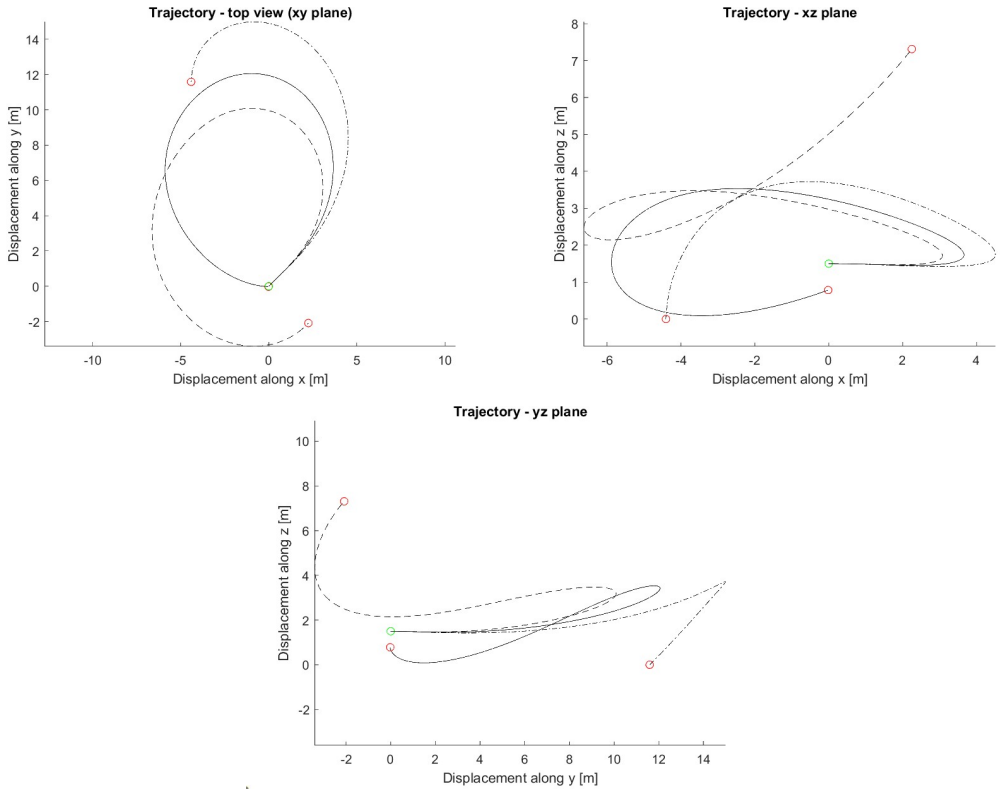

Figure 4.13: —— $l_{blade} = 25$ cm, - - - $l_{blade} = 30$ cm, -·-·- $l_{blade} = 20$ cm

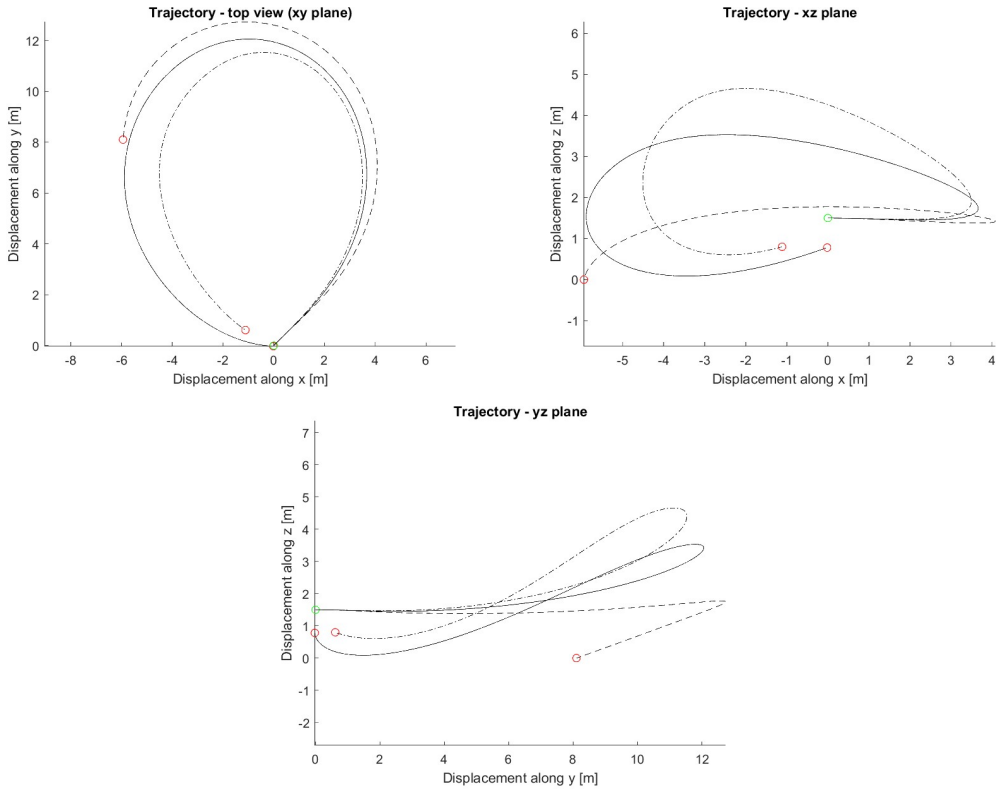

Figure 4.14: —— $\beta = 4°$, - - - $\theta = 8°$, -·-·- $\theta = -0°$

4.6 Wind effects

The wind effects can be taken into account by adding their velocity component to the relative velocity in the wing system. Therefore, equation 4.17 becomes:

$$w = T_j \left(-\vec{v} - \vec{\omega} \times \vec{r} + \vec{v}_i + T_0 V_{wind}\right) \tag{4.26}$$

where V_{wind} is the velocity vector of the wind defined in the inertial frame of reference.

Figure 4.15 shows the effects of winds blowing to the west or the south at a speed of 1.5 m/s, which corresponds to a slight breeze. Even such a low wind speed magnitude remarkably influences the Boomerang's trajectory, with deviations from the undisturbed flight path that are in the order of magnitude of a few meters. The effect on deviation is quite intuitive, with the aircraft reference trajectory that gets dragged into the direction the wind is blowing.

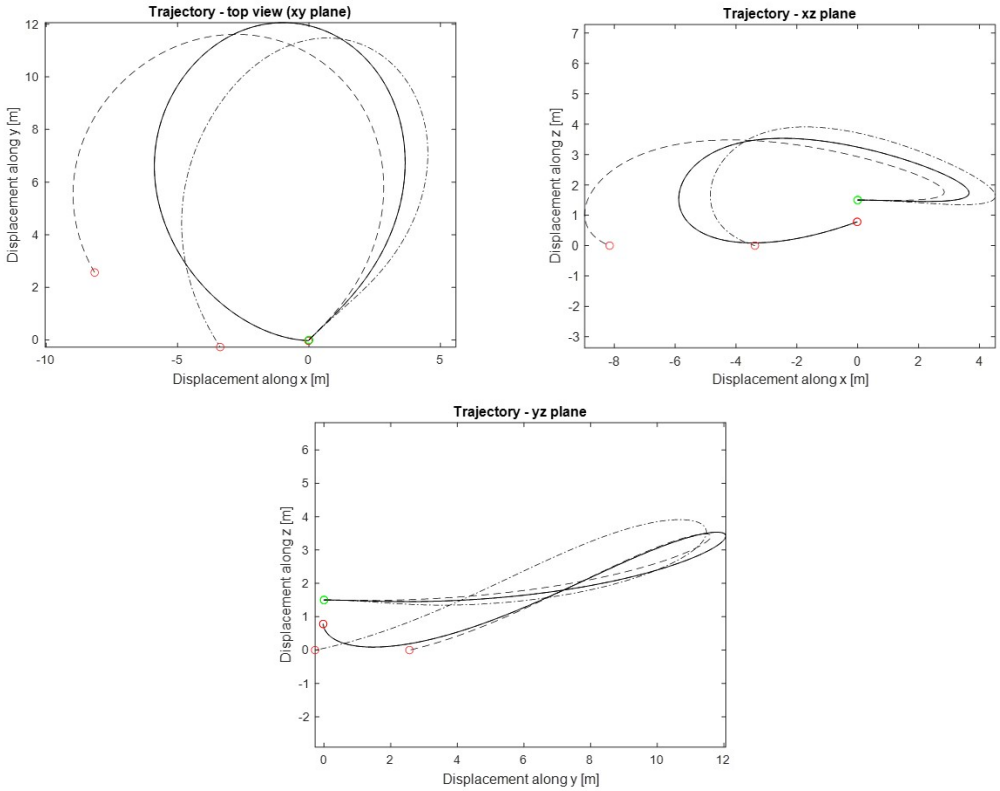

Figure 4.15: —— No wind, - - - Westward wind, -·-·- Southward wind

Blade length	20 cm
Blade chord	4 cm
Launch speed	30 m/s
Launch RPM	600
Launch attitude $[\Phi_0, \Theta_0, \Psi_0]$	[85, 0, 220] °

Table 4.6: Boomerang design and launch parameters for a returning trajectory on Titan

4.7 Planetary Flight

One of the Smart Boomerangs' potential applications is the observation or atmospheric sampling of other planetary bodies with an atmosphere. It is therefore important to know what to expect when a Boomerang is launched into an alien atmosphere, identifying the effects of a different atmosphere density and gravity acceleration on the final trajectory.

4.7.1 Titan

Titan is the second largest moon in the Solar System and one of many Saturn's satellites. It presents a dense atmosphere, primarily composed of nitrogen, and is characterized by the presence of mountains, dunes, lakes, and seas of liquid hydrocarbons. On the surface, its atmosphere is up to 4.4 times as dense as Earth's at sea level [5], and its gravity acceleration is $g = 1.35\ m/s^2$, about a seventh of Earth's. Figure 4.16 shows the trajectory that the same four-wings Boomerang would have if it were to be launched under the same conditions that guarantee return on Earth.
Due to Titan's much denser atmosphere, the flight radius becomes much smaller, decreasing from 12 to around 3 meters. Moreover, the Boomerang tends to spiral upwards due to the low gravity acceleration. A smaller Boomerang launch at a different set of conditions (table 4.6) achieves the trajectory reported in figure 4.17. The Boomerang returns to the initial position, reaching a maximum y of about 5 meters. This means that Smart Boomerang Missions on Titan would require smaller boomerangs than the ones designed for Earth.

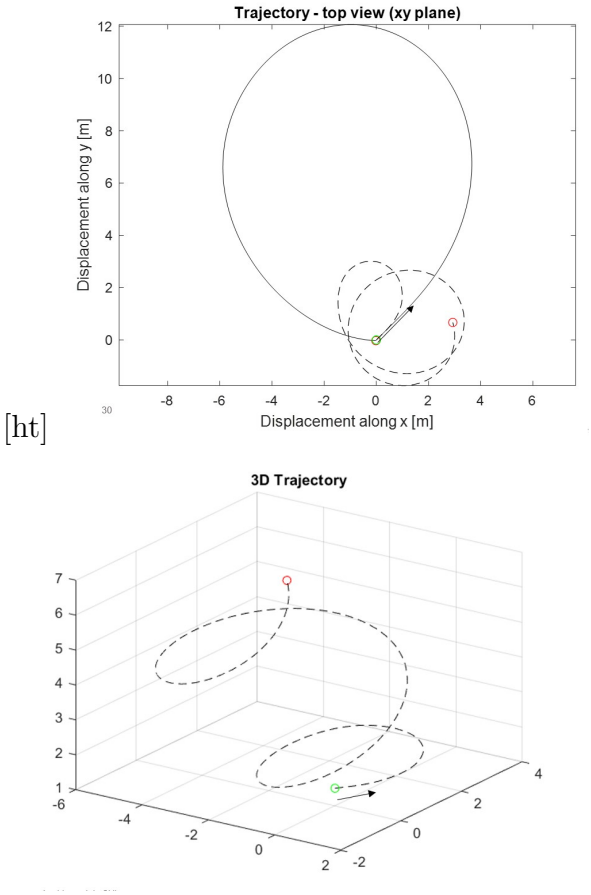

[ht]

Figure 4.16: —— Trajectory on Earth, - - - Trajectory on Titan

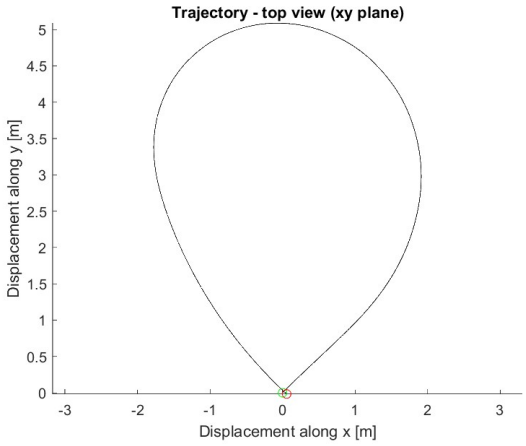

Figure 4.17: Returning trajectory on Titan

4.7.2 Venus at high altitude

Venus is the second planet from the Sun, often considered Earth's sister due to its similar size and composition. Its gravity acceleration is about 10% lower than Earth's at surface level ($g = 8.87\ m/s^2$). However, it presents a dense atmosphere, made up of mostly carbon dioxide and clouds of sulphuric acid. Missions like Venus Aerobot aim to use a balloon to explore the region between 52 and 60 km of altitude, which presents atmospheric conditions similar to Earth. Some of the goals are atmospheric and wind studies, for which a Smart Boomerang Mission could be used, implementing the Launch-and-Capture platform directly on the balloon. For this reason, it is interesting to study a Boomerang's trajectory in the range of altitudes where a Venus Aerobot would fly.

Flight at 52 km

At an altitude of 52 km, Venus' atmospheric density is about $\rho = 1.33 kg/m^3$. Figure 4.18 compares the trajectories that would be obtained on Earth and Venus at this altitude. As the conditions are very similar, the trajectory on Venus results in a slightly smaller maximum y. As shown in figure 4.19, it is possible to obtain a returning trajectory. The only action required is to increase the roll angle at launch, from 75° to 80°.

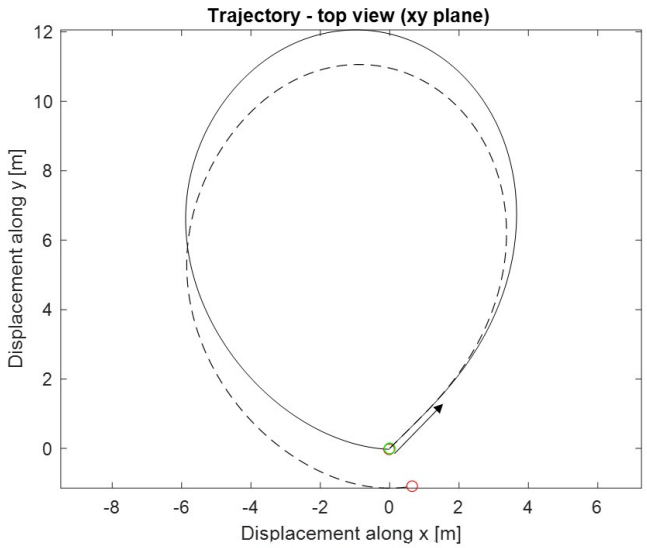

Figure 4.18: —— Trajectory on Earth, - - - Trajectory on Venus at 52 km

Flight at 60 km

At this altitude, the atmosphere is much more thin ($\rho = 0.49\ km/m^3$), being about a third of Earth's at sea level.
In this case, the values of drag and lift produced will be much lower due to the smaller air density. Therefore, the flight will undergo a larger flight path; figure 4.20 shows how the Boomerang starts its returning trajectory at $y = 30$ m, compared to $y = 12m$ on Earth. In the same figure, the trajectory is propagated until the Boomerang loses 1 meter of altitude, after which it is considered to be lost.
In this case, it is necessary to throw a larger boomerang to achieve a returning trajectory within a meter range of altitude difference. Table 4.7 reports the design and launch conditions required.
It is interesting to note that the maximum y achieved by a boomerang varies close to linearly with $1/\rho_{air}$.

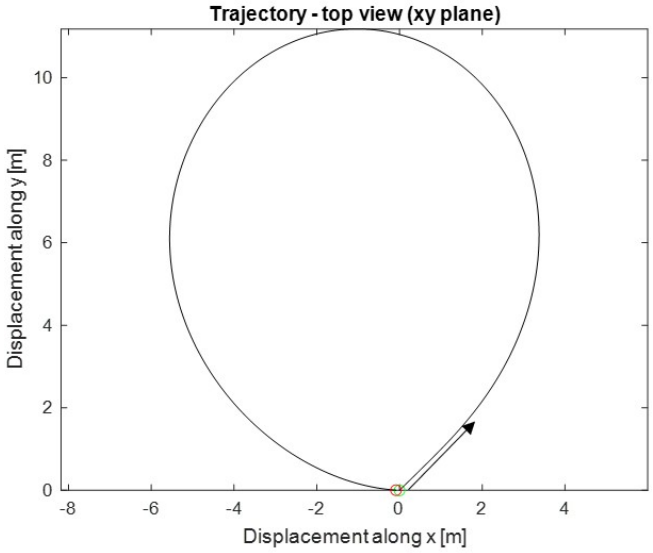

Figure 4.19: Returning trajectory on Venus at 52 km

Blade length	30 cm
Blade chord	6.5 cm
Launch speed	25 m/s
Launch RPM	600
Launch attitude $[\Phi_0, \Theta_0, \Psi_0]$	[80, 0, 220] °

Table 4.7: Boomerang design and launch parameters for a returning trajectory on Venus at 60km

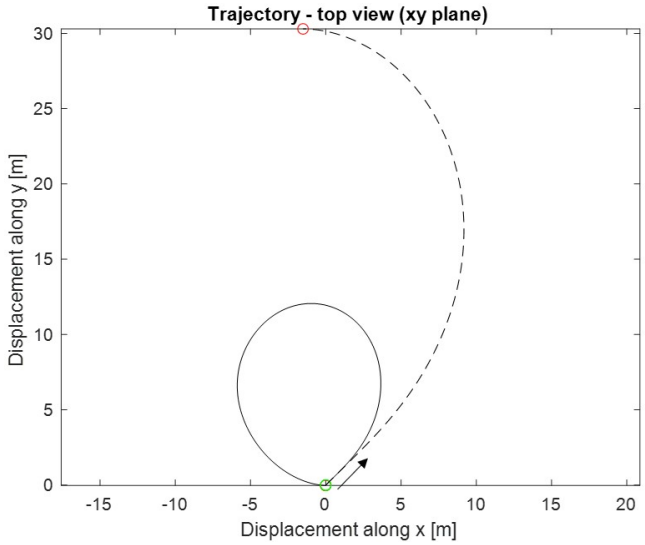

Figure 4.20: —— Trajectory on Earth, - - - Trajectory on Venus at 60 km

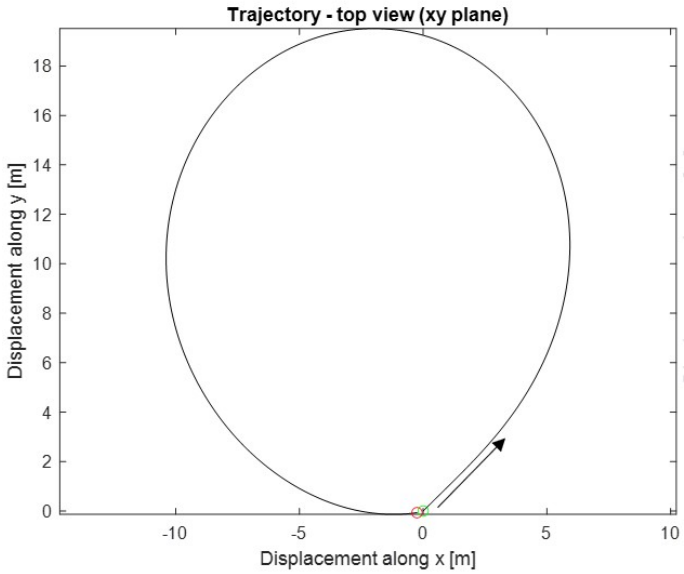

Figure 4.21: Returning trajectory on Venus at 60 km

4.8 Small angles of attack model

It is worth trying an approach that considers small angles of attack. This allows us to analytically solve the equations for computing the lift, resulting in faster computational times. Similar work has been carried out by Vassberg [12], but it will be hereby expanded by including the effects of drag, as well as feathering and torque moments M_2 and M_3. For small angles of attack, the aerodynamic coefficients can be written as [8]:

$$\begin{aligned} C_L &= C_{L0} + C_{L\alpha}\alpha \\ C_D &= C_{D0} + d_1\alpha^2 \\ C_M &= C_{M0} + m_1\alpha \end{aligned} \tag{4.27}$$

where C_{L0}, C_{D0} and C_{M0} are the aerodynamic coefficients for zero angle-of-attack and $C_{L\alpha}$, d_1 and m_1 are constant coefficients that fit the respective aerodynamic coefficient-AoA curve. For small angles of attack, we have:

$$\begin{aligned} \cos\alpha \approx 1,\ \sin\alpha \approx \alpha \\ w_3 \ll w_1 \\ \alpha = \tan^{-1}\left(\frac{w_3}{w_1}\right) \approx \frac{w_3}{w_1} \end{aligned}$$

Therefore, we can approximate equations 4.18 and 4.19 as:

$$\begin{aligned} F^A_{1,j} &\approx \int_{l_r}^{l_t} (-l\alpha + d)d\eta \\ F^A_{2,j} &= 0 \\ F^A_{3,j} &\approx \int_{l_r}^{l_t} (l + d\alpha)d\eta \approx \int_{l_r}^{l_t} l d\eta \end{aligned} \tag{4.28}$$

$$\begin{aligned} M^A_{1,j} &= \int_{l_r}^{l_t} l\eta d\eta \\ M^A_{2,j} &= \int_{l_r}^{l_t} m d\eta \\ M^A_{3,j} &= \int_{l_r}^{l_t} (l\alpha - d)\eta d\eta \end{aligned} \tag{4.29}$$

where, considering that $d \ll l$, the term $d\alpha$ is considered negligible with respect to l.

Another approximation is that the z_b component of the rotational velocity is much larger than the others, so that:

$$w \approx \bar{v}_1 + \omega_3 \eta \tag{4.30}$$

where $\bar{v}_1$ is the first component of the velocity vector $T_j(-\vec{v}$, and the bar will be dropped for simplicity of notation.
By substituting equations 4.16, 4.27 and 4.30 into 4.28 and 4.29, we can derive the expressions for each aerodynamic term.

Derivation of $F^A_{1,j}$

$$\begin{aligned} F^A_{1,j} &= \int_{l_r}^{l_t} \frac{1}{2}\rho c (v_1 + \omega_3\eta)^2(-C_L\alpha + C_D)d\eta = \\ &= \frac{1}{2}\rho c[\int_{l_r}^{l_t} -(v_1+\omega_3\eta)^2 \left(C_{L0} + \cancel{C_{L\alpha}\frac{v_3}{v_1+\omega_3\eta}}\right)\frac{v_3}{v_1+\omega_3\eta}d\eta + \\ &\quad + \int_{l_r}^{l_t}(v_1+\omega_3\eta)^2(C_{D0} + \cancel{d_1\alpha^2})] = \\ F^A_{1,j} &= \frac{1}{2}\rho c\left[-v_3 C_{L0}\left(v_1 l_b + \omega_3\frac{l_b^2}{2}\right) + C_{D0}\left(v_1^2 l_b + v_w\omega_3 l_b^2 + \frac{\omega_3^2 l_b^3}{3}\right)\right] \end{aligned} \tag{4.31}$$

Derivation of $F^A_{3,j}$

$$F^A_{3,j} = \frac{1}{2}\rho c\left[\left(v_1^2 l_b + v_1\omega_3 l_b^2 + \omega_3^2\frac{l_b^3}{3}\right)C_{L0} + \left(v_1 l_b + \omega_3\frac{l_b^2}{2}\right)C_{L\alpha}v_3\right] \tag{4.32}$$

where the terms multiplied by α^2 are canceled being one order of magnitude smaller than the others.

Derivation of $M^A_{1,j}$

$$M^A_{1,j} = \frac{1}{2}\rho c\left[\left(\frac{v_1^2 l_b^2}{2} + \frac{2}{3}v_1\omega_3 l_b^3 + \omega_3^2\frac{l_b^4}{4}\right)C_{L0} + \left(v_1\frac{l_b^2}{2} + \omega_3\frac{l_b^3}{3}\right)C_{L\alpha}v_3\right] \tag{4.33}$$

Derivation of $M^A_{2,j}$

$$M^A_{2,j} = \frac{1}{2}\rho c^2\left[(v_1^2 l_b + \omega_3 v_1 l_b^2 + \omega_3^2\frac{l_b^3}{3})C_{M0} + \left(v_1 l_b + \frac{\omega_3 l_b^2}{2}\right)C_{M\alpha}v_3\right] \tag{4.34}$$

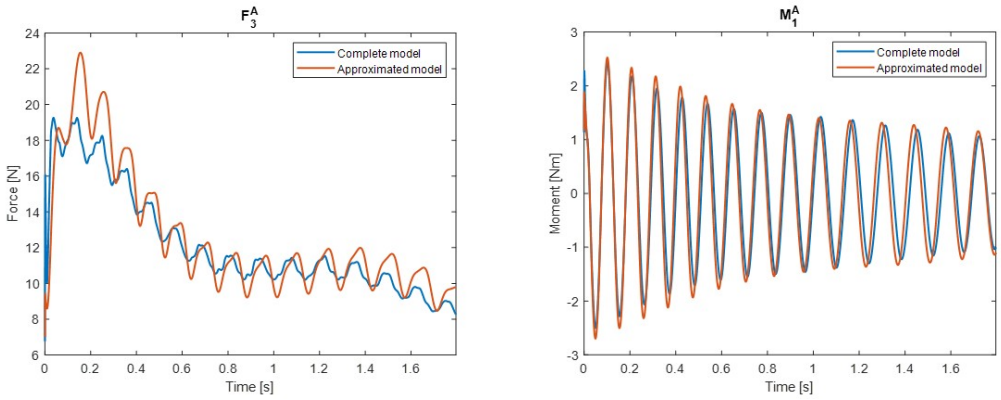

Figure 4.22: Comparison between complete model and small AoAs model - only the forces are approximated

Derivation of $M^A_{3,j}$

$$M^A_{3,j} = \frac{1}{2}\rho c \left[\left(v_1 \frac{l_b^2}{2} + \omega_3 \frac{l_b^3}{3} \right) C_{L0} v_3 - \left(v_1^2 \frac{l_b^2}{2} + \frac{2}{3}\omega_3 v_1 \frac{l_b^3}{3} + \omega_3^2 \frac{l_b^4}{4} \right) \right] \tag{4.35}$$

Finally, we can compare the predictions of the two models. We can do so by comparing the estimates for F_3 and M_1, which are the most influential forces and moments acting on the Boomerang.

Figure 4.22 shows that, if only the aerodynamic forces are computed with the small angles of attack approximation, errors in the computation of forces and moments are quite small and no greater than 10% in relative error.

However, figure 4.23 shows that once the approximation is also applied to the moments, errors become much larger, making the model unsuitable for an accurate prediction. This is because larger errors in the estimation of aerodynamic moments imply larger errors in resulting attitude so that the Boomerang will undergo a different range of angles of attack than in the not approximated case.

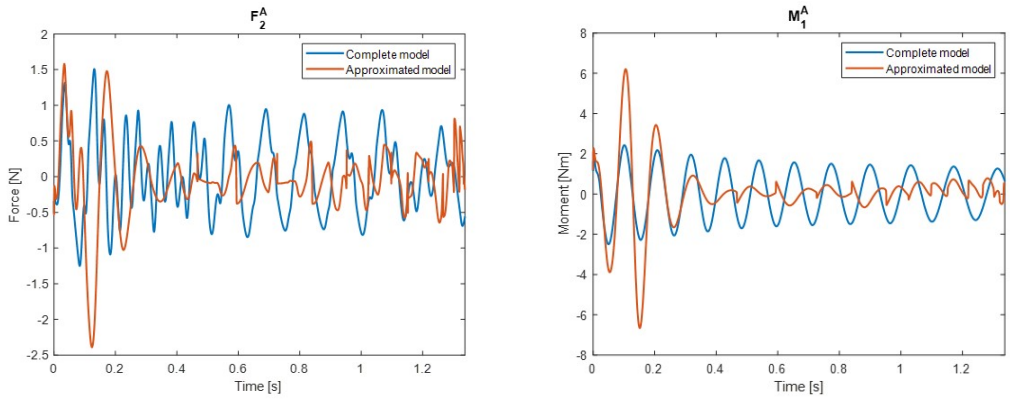

Figure 4.23: Comparison between complete model and small AoAs model - forces and moments are approximated

Chapter 5

Control

This chapter introduces control methods to enhance the trajectories achievable by Standard Boomerangs.
It is important to remember that the Smart Boomerang is an *unpowered probe*, where the only energy for flight is imparted at launch, and it is *underactuated*, as every design solution for trajectory control implements fewer actuators than degrees of freedom.
To approach the control problem, it is necessary to identify the problem statement. In robotics, the problem of motion control can be divided into three main groups [7]:

- **Point stabilization**: move the vehicle to a specific point with a set orientation
- **Trajectory tracking:** the vehicle shall track a reference path with the constraint of time
- **Path following:** the vehicle shall track a reference path without the constraint of time

The Smart Boomerang shall perform a *Path following* mission: the reason is that there are no time constraints or requirements regarding flight time; moreover, the effects of winds could greatly decrease or increase the total flight time of the aircraft, implying the need for a re-parametrization of the set-points. Different control algorithms were considered during the internship:

- Feedback control linearization was deemed not applicable to a real-world case as it requires accurate knowledge of the states as well as forces and moments acting on the boomerang

- Model Predictive Controllers, with current computer technologies, would be too slow to perform controls on an aircraft moving at more than 20 m/s
- Sliding Mode Controllers were discarded for the same reasons as Feedback control linearization

This led to the implementation of a PID controller, which allows preliminary considerations about the extent of the Smart Boomerangs capabilities, and has the potential of being applied in real-world experiments.

5.1 PID Controller logic

The following hypotheses are assumed for the PID controller:

- The Boomerang performs a *Path Following mission:* (see fig. 5.1)

  - No time constraints

  - The desired setpoint is the projection of the boomerang on the desired path

  - Two errors to control: : distance e from the path and angle χ between the current velocity vector in the xy-plane and vector tangent to the path (see fig. 5.1)

- The actuators are considered ideal
- All states are known (ideal state estimation)
- Control is performed at a frequency of 1000 Hz
- Path following is only performed in 2D (in the xy-plane)

The error e and χ are computed as:

$$\varepsilon = [a, e] = R_p^T([X_I, Y_I]^T - [X_{ref}, Y_{ref}]) \tag{5.1}$$

$$\chi = \frac{sin^{-1}(U_x U_{ref,y} - U_y U_{ref,x})}{||U||\,||U_{ref}||} \tag{5.2}$$

with R_p being the rotation matrix that rotates (X_I, Y_I) to (x_{loc}, y_{loc}) and is defined as:

$$R_p = \begin{bmatrix} cos\alpha & -sin\alpha \\ sin\alpha & cos\alpha \end{bmatrix}$$

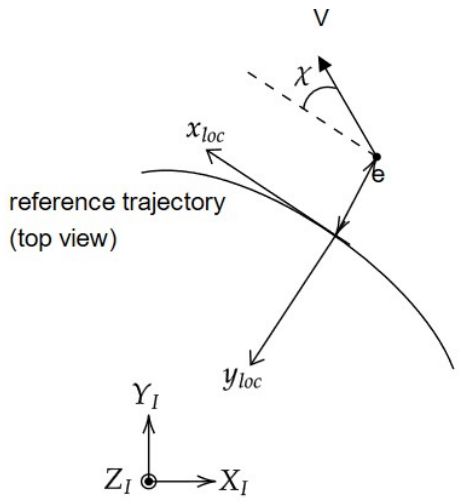

Figure 5.1: Path following scheme

The generic control input is given by:

$$u = K_{p,e}e + K_I \int edt + K_D\dot{e} + K_{p,\chi}\chi \tag{5.3}$$

where u can be the variation of dihedral or pitch angle or blade length, $K_{p,e}$, K_I, K_D are the PID gains for correcting the error e, and $K_{p,\chi}$ is the proportional gain to correct the error χ. The sign of e will be negative (positive) if the flight radius needs to decrease (increase). This means that:

- When considering pitch control, e will be multiplied by -1 $(+1)$ to increase (decrease) the pitch angle and thus decrease (increase) the flight path radius

- When considering dihedral angle control, e will be multiplied by $+1$ (-1) to increase (decrease) the dihedral angle and thus decrease (increase) the flight path radius

- When considering blade length control, e will be multiplied by -1 $(+1)$ to increase (decrease) the blade length and thus decrease (increase) the flight path radius

Figures 5.2 and 5.3 summarize in a scheme the control algorithms just described.

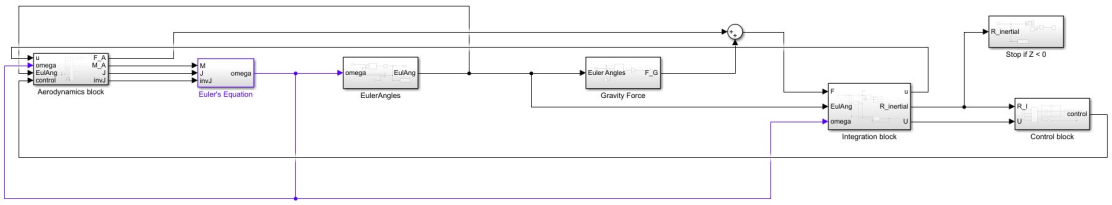

Figure 5.2: Control scheme

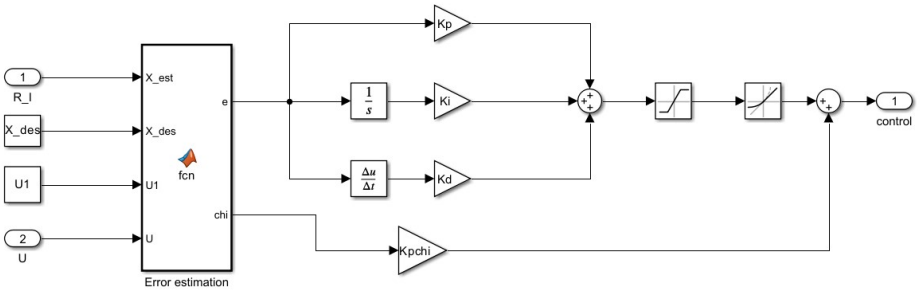

Figure 5.3: Generation of the control input

5.1.1 Control techniques comparison

The performances of the three methods listed in Chapter 1 and reported in figures 1.4, 1.5, and 1.6 are compared.
The case study's mission is to complete a returning trajectory under the influence of a westward wind blowing at 1.5 m/s. The reference path is the returning one that the Boomerang would achieve in undisturbed conditions - the same one computed in Chapter 4. For each case study, launch conditions and boomerang design are kept constant. Each control signal has a rate of change limit given by the maximum rotation speed of a COTS servo motor that could be used as an actuator, which is considered to be 500 RPM. Constraints on maximum and minimum control signals are also considered thanks to Simulink's saturation block:

- The maximum pitch is $\theta_{max} = 40°$, while the minimum one is $\theta_{min} = -5°$. This range is given from values adopted for helicopter rotors [9], with the lower limit being reduced to just $-5°$ to limit losses of lift during flight
- The maximum dihedral angle is $\beta_{max} = 10°$, while the minimum one is $\beta_{min} = 0°$. This limit is based on mechanical considerations.
- The range of blade length variation is ± 5 cm. This range is based on the proposed wing design.

The results obtained are shown in figures 5.4, 5.5, and 5.6. We can see that:

- Wing pitch control allows for a quite accurate path following during the first phase of the launch, after which the maximum pitch is achieved and the Smart Boomerang tries to track the reference path
- Dihedral angle control is the least promising, with the Smart Boomerang struggling to follow the reference path
- Blade length control also delivers promising results, while being less accurate than wing pitch control during the first phase of launch

However, none of the proposed methods allows for the Boomerang to return to the initial point: in each of the three cases, the aircraft impacts the ground before completing the mission.
These results show that it is necessary to introduce an altitude control, as well as enhance the Smart Boomerang capabilities by leveraging Attitude Control.

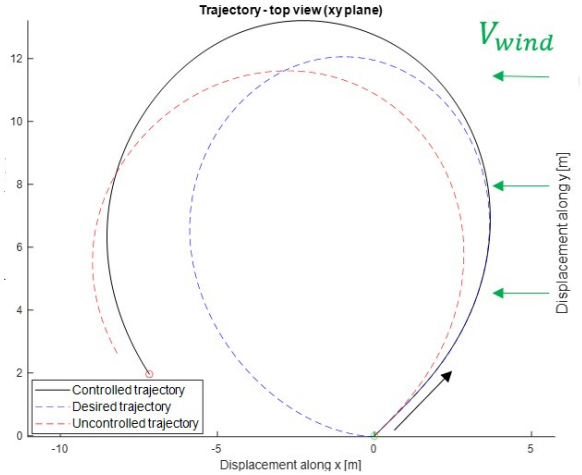

Figure 5.4: Path Following through pitch control

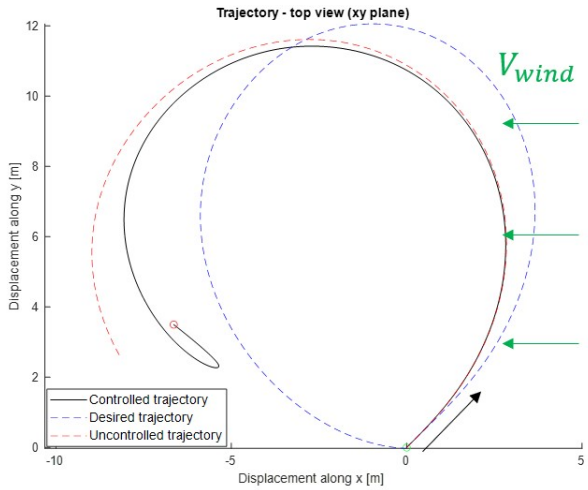

Figure 5.5: Path Following through dihedral angle control

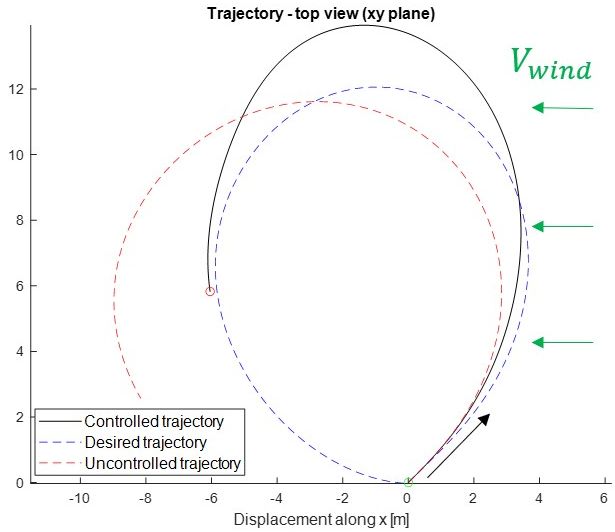

Figure 5.6: Path Following through blade length control

5.2 Enhancement through Attitude Control

Helicopters achieve attitude control thanks to cyclic pitch variations of their blades. The same method will be used for the Smart Boomerang attitude control, with the assumption that each blade can be controlled independently from one another. This assumption implies that the proposed Smart Boomerang design needs to be updated, but this will be an object for future work. Moreover, the analysis will be focused on the wing pitch control method, as it guaranteed promising results and it would be easier to build a Smart Boomerang prototype that can achieve both collective and cyclic pitch control rather than mixing control methods.
The wing pitch at an azimuth angle of blade rotation will therefore be given by:

$$\theta = \theta_0 + \theta_c cos(\psi) \tag{5.4}$$

where θ_0 is the collective pitch, θ_c is the cyclic pitch, and ψ is the azimuth angle as shown in picture 5.7. The control logic is the following:

- Wing pitch increases (decreases) to:
  - Rotate the velocity vector counter-clockwise (clockwise)
  - Increase (decrease) e if $e < 0$ ($e > 0$)
  - Recover height if $Z_I < Z_{I,0}$ ($Z_{err} = Z - Z_{I,0}$)

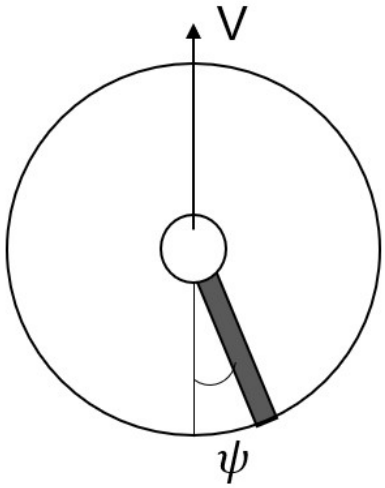

Figure 5.7: Azimuth angle of the blade

- Roll angle decreases to:
  - Rotate the velocity vector clockwise
  - Decrease e if $e > 0$
  - Recover height if $Z_I < Z_{I,0}$

Therefore, the control actions are defined as:

$$\theta_0 = K_{p\theta,e}e + K_I \int edt + K_D\dot{e} + K_{p\theta,\chi}\chi + K_{p\theta,z}Z_{err} \tag{5.5}$$

$$\theta_c = K_{p\phi,e}e + K_{p\phi,\chi}\chi + K_{p\phi,z}Z_{err} \tag{5.6}$$

This control logic proved to be successful: figure 5.8 shows that the Path Following mission is completed, and the Smart Boomerang returns to the Launcher before hitting the ground. In figure 5.9, we can see that even under a different wind condition (wind blowing to the south) the mission is carried out successfully, using the same gains as the first case.
Figures 5.10, 5.11, and 5.12 show wind conditions that do not allow the Boomerang to come back to its initial position. In the former case, the wind magnitude is increased up to 3 m/s and deemed too strong of a gust for the Boomerang to fully counteract it. In the two latter cases, the wind is blowing *in favor* of the Smart Boomerang at launch: this means that the Boomerang will be blowing *against* the Boomerang on the returning phase of its trajectory, at which time the aircraft will have lost most of its kinetic and rotational energy. In these cases, an unpowered

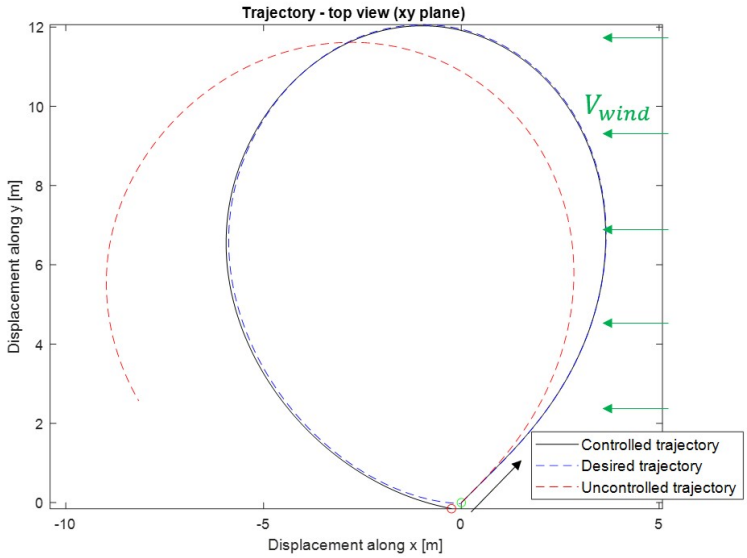

Figure 5.8: Example of a successful mission: the Smart Boomerang returns to the thrower under the influence of a westward wind

Smart Boomerang would be incapable of returning to the launcher.
It is therefore imperative to measure the winds during a Smart Boomerang Mission: not only high wind speeds but also wind direction will deeply affect the resulting flight, making it impossible to recover the probe under unfavorable conditions.

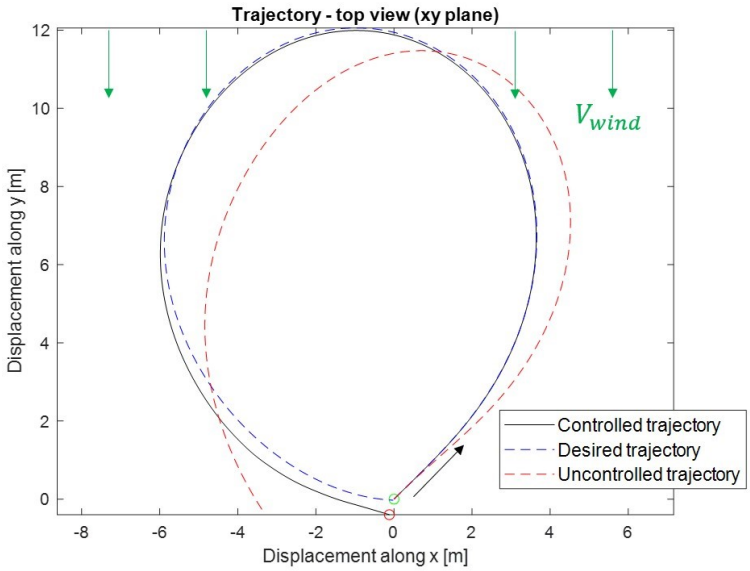

Figure 5.9: Example of a successful mission: the Smart Boomerang returns to the thrower under the influence of a southward wind

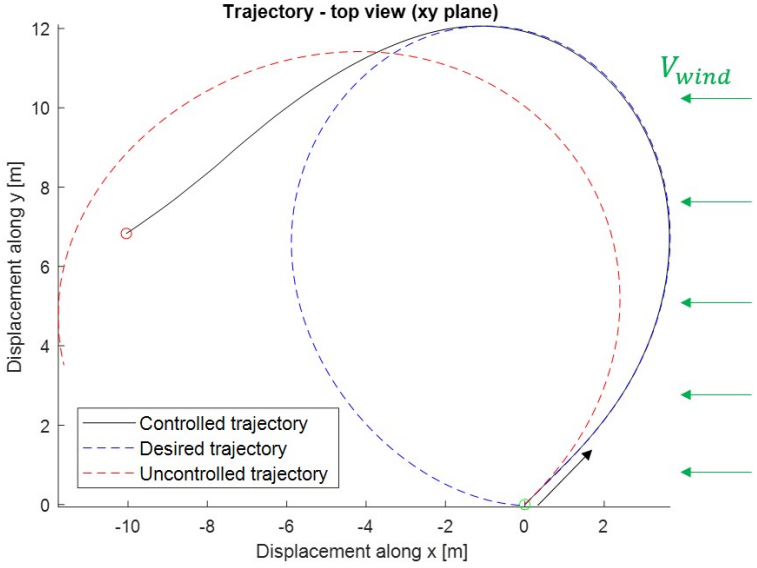

Figure 5.10: Example of an unsuccessful mission: the Smart Boomerang falls to the ground under the effects of a westward but stronger wind, blowing at 3 m/s

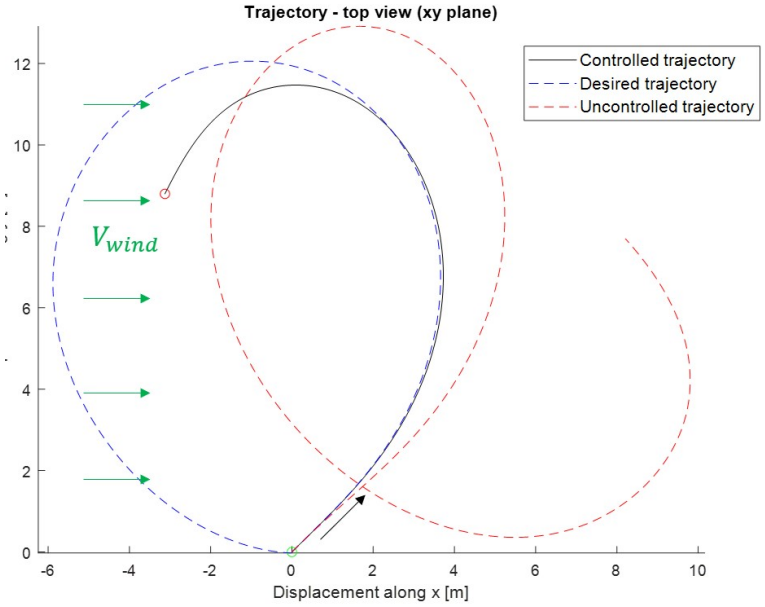

Figure 5.11: Example of an unsuccessful mission: the Smart Boomerang falls to the ground before returning to the Launcher under the effects of an eastward wind

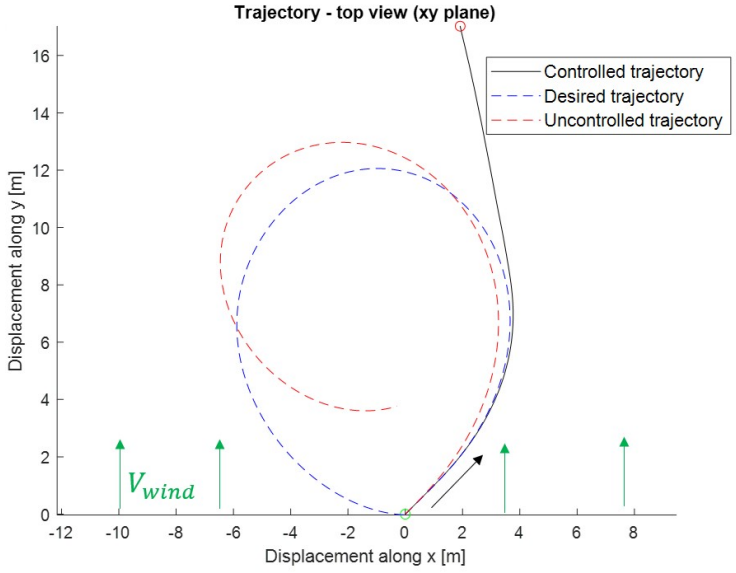

Figure 5.12: Example of an unsuccessful mission: the Smart Boomerang falls to the ground before returning to the Launcher under the effects of an eastward wind

Chapter 6

State estimation

In Chapter 5, it was stated that one of the assumptions made when studying the Path Following capabilities of Smart Boomerangs was that all of the states were fully known.
In a first attempt to define the requirements for the design of an Autonomous Smart Boomerang, it is essential to understand how to perform the full State Estimation of the aircraft.
For the Path Following purposes, the main states to be estimated are:

- **Position**. In a first design iteration, we can define the following requirement: "*The error on position estimation shall be less than 1 meter at the moment of capture*". This would allow the boomerang to come back to the Launch-and-Capture Platform within 1 meter of it, which could be enough for the Capture system to catch the Boomerang back.
- **Linear velocity**
- **Attitude**
- **Rotational velocity**

It is therefore necessary to understand what sensors could be capable of satisfying the state estimation requirements.

6.1 Sensors for State Estimation

In the robotic field, a wide range of sensors can be used for State Estimation. Some examples are:

- **GPS Sensors**: usable for position estimation. However, a GPS Sensor would only work on Earth; moreover, it only allows for position estimate accuracies of about 3 meters, making it incompatible with the defined requirements.

- **Cameras**: by acquiring photons during the exposure time, cameras generate 2D images that can be used for perception purposes. Their frequency output is low, in the range of hundreds of Hz.

- **Inertial Measurement Units (IMUs)**: these sensors make use of an accelerometer, a gyroscope, and sometimes a magnetometer to measure the acceleration and rotational speed of an object (and its orientation in case a magnetometer is integrated). IMUs have to advantage of being scene-independent sensors and having high output frequencies (in the range of thousands of Hz). However, they suffer from poor signal-to-noise ratios at low accelerations and angular velocities and biases in measurements make position estimates drift quickly as errors are integrated twice in time to obtain a position estimate .[11].

Cameras and IMUs are complementary sensors that are often used together: this is called Visual Inertial Odometry.
However, equipping a camera on a boomerang might present multiple issues:

- Added weight to the Smart Boomerang

- *High Dynamic Range (HDR) and Motion Blur problems*: as the camera is mounted on a spinning object like a Boomerang, images might be unusable due to under- or over-exposure caused by HDR or Motion Blur due to the high-speed rotations at which the camera spin along with the Boomerang

Given that a Smart Boomerang flight usually lasts less than 10 seconds, it is worth trying to see if IMU sensors could be used on their own.

6.2 IMU Modeling

Two important requirements can be defined for the specifics of an IMU that is going to be mounted on a Boomerang:

1. The accelerometer shall have a measurement range of at least $\pm$ 12 g

2. The gyroscope shall have a measurement range of at least ± 4000°/s

These specifications are required as these are the ranges of accelerations and rotational velocities that a Boomerang usually experiences during flight.
To perform a preliminary analysis, a commercially available IMU that respects these requirements is selected and modeled in Simulink. Its properties are:

- **Sampling frequency:** 1000 Hz
- **Accelerometer properties**:

  Scale factor[1]**:** 1

  Cross couplings[2]**:** 0.5%

  Bias[3]**:** 60e-3 g

  Measurement Range: ±16 g

  Noise Power: 22.4 $\frac{\mu m}{s^2}/Hz$

- **Gyroscope properties:**

  Scale factor: 1

  Cross couplings: 1%

  G-bias[4]: 0.1°/s

  Bias: 3°/s

  Measurement Range: ±4000°/sec

The inputs to the IMU block are:

- The angular velocity ω
- The acceleration in body axes: $a_b = \dot{v} + v \times \omega$

and the outputs are the measured angular velocity and acceleration. Position, linear velocity, and attitude are estimated by integration.

[1]Rate between input and output
[2]Accelerations in a given direction also influence measurements in the other axes
[3]Output level when no acceleration is measured, given by different factors such as bad calibration, temperature changes
[4]Takes in account a shifting bias from which gyroscopes suffer when a linear acceleration is applied

6.3 Results analysis

As can be seen in figures 6.1 and 6.2, measurements of accelerations and angular velocities are performed quite accurately by the IMU, as they are directly measured by the sensor. Errors in estimation are mainly caused by bias and noise. However, errors in velocity, position, and attitude estimation are expected to be much larger, as these quantities will not be obtained directly, but through numerical integration of the measured accelerations and angular velocities. Indeed, if a_m is the measured acceleration, we can say that:

$$a_m = a_{real} + e$$

where e generically indicates estimation errors due to noise and bias. Therefore, the velocity and position estimates will be:

$$v_m = a_m * \Delta t = a_{real} * t + e * t$$
$$pos_m = \frac{1}{2}(a_m \Delta t) = \frac{1}{2}(a_{real} * t^2 + e * t^2)$$

therefore, integrating once implies that there will be an additional measurement error that grows linearly with time while integrating twice implies a quadratic additional error with time.
Indeed, figure 6.3 shows how the error on linear velocity estimation grows linearly with time, with oscillations due to noise. On the other hand, figure 6.4 shows that the error on position estimation grows quadratically and becomes larger than 1 meter after less than one second. Errors in attitude estimation also tend to quickly grow to over 300 degrees in just half a second, only to decrease as the boomerang slows down in translational velocity and rotation. Therefore, it is shown that the requirement for position estimation is not respected, and an IMU sensor would require correction at least every half of a second to reset errors in position and attitude estimation.
It is proved that further work and analyses need to be carried out about the state estimation problem. Some possible solutions could be:

- Use of **event cameras**: this innovative type of sensor gathers data by measuring the changes in luminosity given by each pixel of the image. This allows to overcome the problems of High Dynamic Range and Motion Blur. These could be the ideal sensors to mount on an object that is moving and spinning at a high rate like a Boomerang

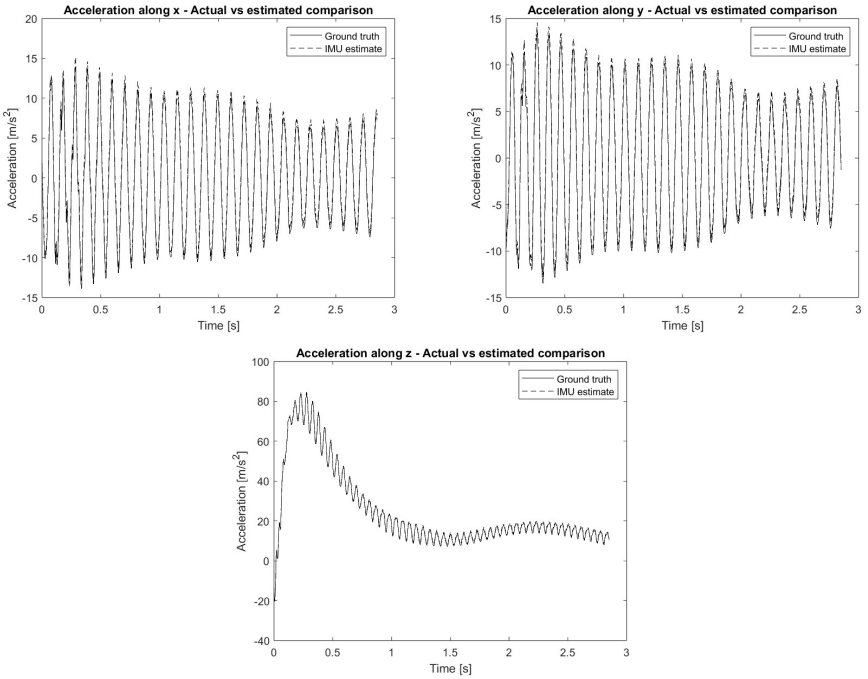

Figure 6.1: Comparison between actual and measured accelerations

- Use a set of cameras mounted on the launcher
- Use other sensors like RADARs, LiDARs, or Ultra-Wideband

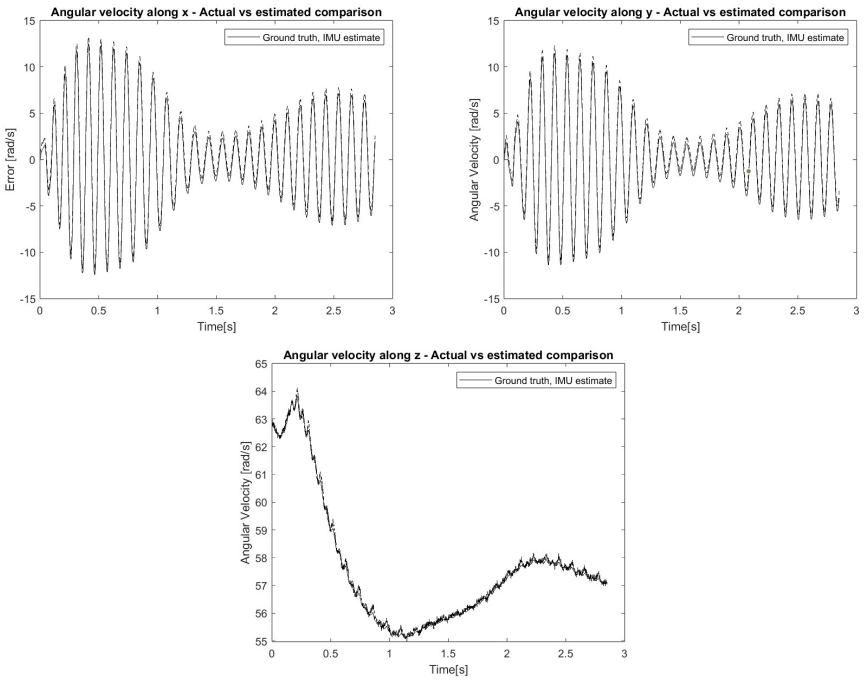

Figure 6.2: Comparison between actual and measured angular velocities

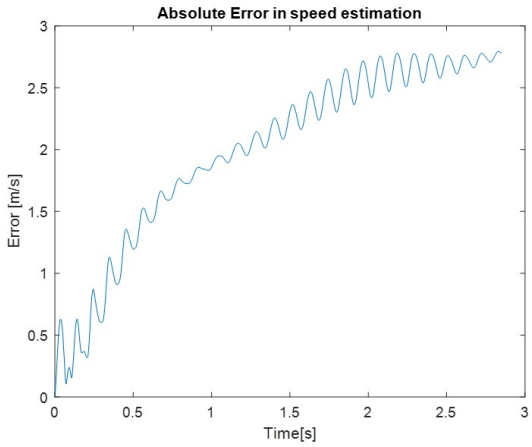

Figure 6.3: Error on velocity estimation

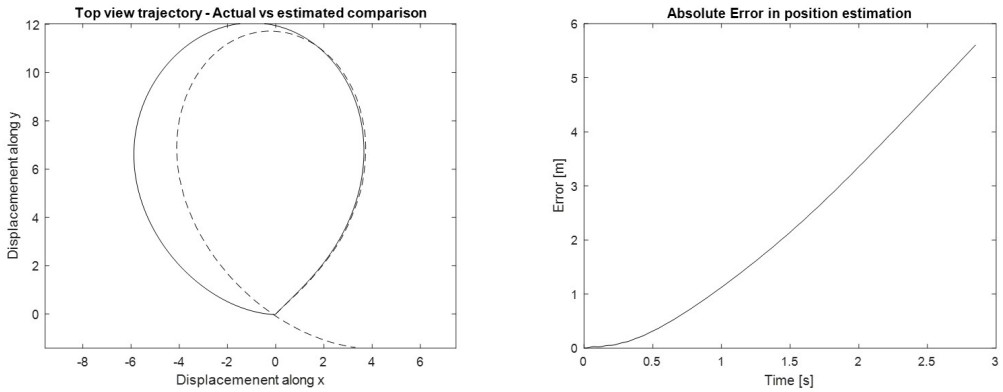

Figure 6.4: Position estimation from IMU data integration

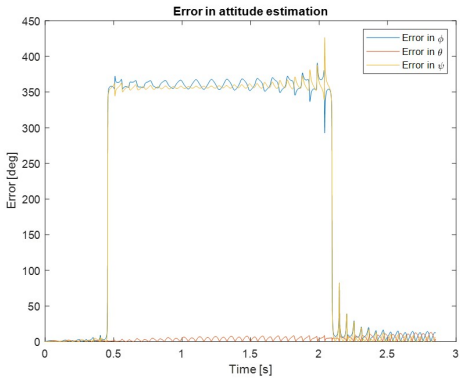

Figure 6.5: Error on attitude estimation

Chapter 7

Conclusions

During the previous chapter, there was much space left for future work on this innovative type of aircraft that could be used for planetary exploration, and many considerations were drawn about Boomerangs, Smart Boomerangs, and Smart Boomerang Missions.

7.1 Future work

Future suggested work comprises:

- Wind-Tunnel experiments for better estimation of aerodynamic forces in simulations
- Introduction of optimal control methods
- Further studies on state estimation
- Improve the Smart Boomerang design and implement a prototype with cyclic pitch control
- Develop algorithms to automatically find launch conditions that guarantee a returning trajectory
- Introduce motion planning or online generation of reference trajectories, useful for tracking a target

7.2 Summary

It is worth to gather the most important conclusions drawn during the work, which were:

- The Smart Boomerang prototypes built during the internship require a dedicated launcher
- The developed simulator is capable of predicting a Boomerang's trajectory, given its design and launch parameters
- Launch conditions, Boomerang design, and environmental conditions heavily influence the resulting trajectory

  - Decreasing (increasing) the roll angle implies reaching higher (lower) altitudes, with the Boomerang landing to the back (to the front) of the thrower

  - Larger (smaller) Boomerangs produce more (less) lift and therefore fly with a smaller (larger) flight trajectory

  - The flight radius varies close to inversely proportional to air density, which is useful when planning flights on other planets
- The wing-pitch control system allows for accurate path-following

  - It needs to be enhanced with attitude control capabilities (cyclic pitch control)

  - During a Smart Boomerang Mission, measurements of wind conditions shall be performed before launching the boomerang, to guarantee favorable conditions for the return of the probe
- The Smart Boomerang probe shall be able to perform position estimation with an error of ¡1 m

  - IMU sensors cannot be used as the only means of measurements

  - Event cameras could be a complementary sensor to IMUs

Bibliography

[1] Kinematics Handout, MIT Engineering Dynamics, Fall 2010.

[2] Spacecraft Attitude Dynamics and Control, Notes for the Satellite Attitude Dynamics and Control course at Politecnico di Torino, 2008-09.

[3] A Azuma et al. "Flight Dynamics of the Boomerang, Part 1: Fundamental Analysis". In: *Journal of Guidance, Control and Dynamics* (2004).

[4] G. Beppu et al. "Flight Dynamics of the Boomerang, Part 2: Effects of Initial Conditions and Geometrical Configuration". In: *Journal of Guidance, Control and Dynamics* (2004).

[5] A. Coustenis. "The origin and evolution of Titan's atmosphere". In: *Department of Space Research and Instrumentation in Astrophysics (LESIA), Paris-Meudon Observatory* ().

[6] Felix Hess. *Boomerangs, Aerodynamics and Motion*. University of Groningen, 1975.

[7] L. Lapierre and A. Pascoal. "Nonsingular Path Following Control of a Unicycle in the Presence of Parametric Modelling Uncertainties". In: *International Journal of Robust and Nonlinear Control* (2006).

[8] J. G. Leishman. *Principles of Helicopter Aerodynamics*. Cambridge University Press, 2006.

[9] A. Levin and R. Smith. "Experimental Aerodynamic Performance Characteristics of a Rotor Entry Vehicle Configuration". In: *NASA Ames Research Center* (1971).

[10] Bernard S. Mason. *Boomerangs - How to make & Throw Them*. Dover Publications, 1974.

[11] D. Scaramuzza and Z. Zhang. "Visual-Inertial Odometry of Aerial Robots". In: *Encyclopedia of Robotics, Springer* (2019).

[12] J. Vassberg. "Boomerang Flight Dynamics". In: *30th AIAA Applied Aerodynamics Conference* (2012).